

Experimental Characterization and Modeling of Wettability in Two Phase Oil/Water
Flow in the Annular Flume Apparatus

A thesis presented to
the faculty of
the Russ College of Engineering and Technology of Ohio University

In partial fulfillment
of the requirements for the degree
Master of Science

Kevin T. Blake

May 2019

© 2019 Kevin T. Blake. All Rights Reserved.

This thesis titled
Experimental Characterization and Modeling of Wettability in Two Phase Oil/Water
Flow in the Annular Flume Apparatus

by

KEVIN T. BLAKE

has been approved for

the Department of Mechanical Engineering

and the Russ College of Engineering and Technology by

Marc Singer

Associate Professor of Chemical Engineering

Dennis Irwin

Dean, Russ College of Engineering and Technology

ABSTRACT

BLAKE, K., M.S., May 2019, Mechanical Engineering

Experimental Characterization and Modeling of Wettability in Two-Phase Oil/Water flow in the Annular Flume Apparatus

Director of Thesis: Dr. Marc Singer

This thesis documents the hydrodynamic characterization of an apparatus called the annular flume apparatus. It is designed to simulate pipeline flow in a small-scale setting, making experimentation of oil/water two-phase flow more timely and efficient than traditional testing. Predicting water wetting in two-phase oil/water flow of the bottom surface of the pipeline is essential in preventing corrosion. The current water wetting model used to predict water wetting at the Institute for Corrosion and Multiphase Technology is based on two-phase oil/water flow data from a 4 in. ID, 40m long flow loop. Due to its size, experimentation in the flow loop requires extensive time, manpower, and volumes of fluid. To make experimentation more efficient, the annular flume apparatus was designed; however, it is unclear whether this apparatus provides an accurate representation of pipeline flow. Pipe flow is pressure driven and annular flume flow is shear driven by a rotating top plate. More specifically, annular flume flow exhibits a gradient in shear stress from the top of the conduit to the bottom.

Shear stress is a crucial parameter in the water wetting model as it helps determining the critical droplet size (considering water droplets dispersed in oil) and is essential in defining the transition between flow/wetting regimes. In order to predict shear stress, the water wetting model for horizontal pipe flow uses a single expression of

the Fanning friction factor, while this study provides two Fanning friction factors for the annular flume apparatus: f_{top} for the top of the conduit, and f_{bottom} for the bottom of the conduit. The Fanning friction factors can be used in evaluating the stability of dispersed flow and determining phase wetting regimes in the annular flume in a timely manner, using only the physical properties of the fluids and the mean tangential velocity of the rotating top plate.

Comprehensive knowledge of flow within the annular flume requires numerical modeling of multiphase flow. Because numerical modeling of multiphase flow is so complex, the first step towards this is modeling of single phase flow. The goal of this study was to characterize the hydrodynamics of the annular flume, perform numerical modeling of single phase flow in the annular flume to produce computational fluid dynamics (CFD) simulations and validate these simulations with experimental hydrodynamic measurements; namely, tangential velocity (m/s) and wall shear stress (Pa) of fluid flow in the annular flume, as well as phase wetting. The $k - \varepsilon$ turbulence model was used for the CFD simulations. The results of the CFD simulations were then used to visualize the flow characteristics in the annular flume and to modify a key parameter of the water wetting model; namely, the Blasius type correlation for a Fanning friction factor.

DEDICATION

This work is dedicated to my family.

ACKNOWLEDGMENTS

I would especially like to thank Dr. Marc Singer for his endless assistance and his patience through this entire process. I would like to thank the staff at the ICMT, including Dr. Luciano Paolinelli, Alexis Barxias, Cody Shafer, and Al Schubert for their tremendous help. I would like to thank my committee – Dr. Pasic, Dr. Trembly, Dr. Bayless, Dr. Held, and Dr. Singer for helping with the completion of my thesis. I would then like to thank Ohio University for making this possible and Dr. Srdjan Nestic for his support. Lastly, I would like to thank my family for the help that each of them provided me throughout this process.

TABLE OF CONTENTS

	Page
Abstract	3
Dedication	5
Acknowledgments	6
List of Tables.....	9
List of Figures	10
Glossary	12
Introduction.....	14
Background	18
2.1. Water Wetting Fundamentals	18
2.2. Predicting the Transition from Dispersed Flow	19
2.3. ICMT Water Wetting Model	23
2.4. Flow Characteristics in Annular Flume Apparatus.....	30
Project Objectives.....	38
Scope of Work and Test Matrices	40
4.1. Scope of Work	40
4.1.1. Range of Fluid Properties Used in the Study	40
4.1.2. Scope of the Hydrodynamic Study	41
4.1.3. Scope of Phase Wetting Study	41
4.1.4. Scope of Numerical Modeling.....	42
4.2. Test Matrices.....	42
Experimental Setup and Procedures	44
5.1. Annular Flume Setup.....	44
5.2. In Situ Circumferential Velocity.....	46
5.2.1. Pitot Tube Calibration Procedure	47
5.2.2. Pitot Tube Experimental Procedure	48
5.3. Wall Shear Stress	49
5.3.1. Wall Shear Stress Probe Preparation Procedure.....	51
5.3.2. Wall Shear Stress Experimental Procedure.....	51
5.4. Phase Wetting Determination Procedure.....	52
5.4.1. Phase Wetting Procedures.....	53
5.4.2. Phase Wetting Preparation Procedure.....	54
5.4.3. Safety (disposal)	56
Experimental Results and Discussion.....	57
6.1. Hydrodynamic Study: Velocity Profiles	57
6.2. CFD Model Parameters	63
6.3. Validation of CFD Model: Velocity Results	65
6.4. Modeling of Tangential and Transverse Flow in the Annular Flume	69
6.4.1. Modeling of Tangential Flow.....	69
6.4.2. Modeling of Transverse Velocity	71
6.5. Hydrodynamic Study: Wall Shear Stress Profiles	73
6.6. Validation of CFD Model: Bottom Wall Shear Stress	76

6.7. Modeling of Bottom Wall Shear Stress.....	78
6.8. Discrepancies between Model Results and Experimental Results for Shear Stress.....	79
6.9. The Effect of the Gap between the Top Plate and the Outer Wall on Flow Velocity and Shear Stress.....	82
6.10. Phase Wetting Maps.....	84
6.11. Determination of Blasius Type Correlations	87
Recommendations	89
Conclusions and Future Work.....	90
References	90
Appendix 1: $k - \epsilon$ Turbulence Model.....	97
Appendix 2: Calculation of Vertical Velocity Component of Transverse Flow	99

LIST OF TABLES

	Page
Table 1. Fluid properties (model oils and water) used in experimentation.	41
Table 2. Test matrix of annular flume tests for hydrodynamic measurements in single phase flow	43
Table 3. Test matrix for phase wetting experiments in two-phase flow.....	43

LIST OF FIGURES

	Page
Figure 1. Diagram of stratified flow in two phase oil-water pipe flow, wherein water (blue), and oil (yellow) flow in segregated layers.	18
Figure 2. Diagram of dispersed flow in two phase oil-water pipe flow wherein the water phase (blue) is fully dispersed in droplets entrained by the oil phase (yellow).	19
Figure 3. Diagram of turbulent force, FT , and gravitational force, FG , acting on a dispersed phase droplet.	20
Figure 4. Depiction of turbulent breakup of dispersed phase droplets (Yao, 2016).	23
Figure 5. Cross section of annular flume experimental setup (Gardner, 2017).	45
Figure 6. Diagram of the Pitot tube used to measure differential pressure.	47
Figure 7. Calibration curve for Pitot tube setup.	48
Figure 8. Depiction of Lenterra Wall Shear Stress Probe (Sheverev, 2012).	50
Figure 9. Wall conductance probe made by inserting a stainless steel wire coated in epoxy into a stainless steel sleeve.	53
Figure 10. CAD drawing of the stainless bottom plate of the annular flume with large ports for a wall shear stress probe and a Pitot tube, respectively, and 12 rows of 8 ports for conductance probes (Albert Schubert of the ICMT).	53
Figure 11. Plot of experimental results of tangential velocity profiles of brine at varying heights and top plate speeds in the 2.0 in. conduit.	58
Figure 12. Plot of experimental results of tangential velocity profiles for the brine at varying heights and top plate speeds in the 4.5 inch conduit.	58
Figure 13. Plot of experimental results of tangential velocity profiles for the LVT 200 at varying heights and top plate speeds in the 2.0 in. conduit.	59
Figure 14. Plot of experimental results of tangential velocity profiles for the LVT 200 at varying heights and top plate speeds in the 4.5 inch conduit.	60
Figure 15. Plot of experimental results of tangential velocity profiles for the Isopar-V at various rotating top plate speeds in the 2.0 in. conduit.	62
Figure 16. Plot of experimental results of tangential velocity profiles for the Isopar-V at varying heights and top plate speeds in the 4.5 in. conduit.	62
Figure 17. A profile of the rectangular cross-section of the mesh used in the current study.	64
Figure 18. Left: Top view of the CFD mesh used in the current study. Right: Magnified view of top mesh of current study.	65
Figure 19. Plot of model results and experimental results single phase tangential flow velocities of DI water + 1% NaCl at varying heights for top plate rotational speeds of 87.8 RPMs, 163.4 RPMs, and 210.3 RPMs. Model results are plotted as smooth, solid lines. Experimental results are plotted as points along a dashed line.	67
Figure 20. Plot of model results and experimental results single phase tangential flow velocities of LVT-200 at varying heights for top plate rotational speeds of 87.8 RPMs, 163.4 RPMs, and 210.3 RPMs.	68

Figure 21. Plot of model results and experimental results of single phase tangential flow velocities Isopar-V at varying heights for top plate rotational speeds of 87.8 RPMs, 163.4 RPMs, and 210.3 RPMs.....	69
Figure 22. Model results: Contour of tangential velocity of Isopar-V flow across the conduit at a top plate rotational speed of 87.8 rpm.	70
Figure 23. Model results of transverse velocity (m/s) vector field for Isopar-V at a top plate rotational speed of 87.8 rpm.	73
Figure 24. Experimental results of average bottom wall shear stress plotted as a function of top plate rotational speed with the conduit height of the annular flume set to 2.00 in.	75
Figure 25. Experimental results of average bottom wall shear stress plotted as a function of top plate rotational speed with the conduit height of the annular flume set to 4.5 in.	76
Figure 26. Model Results plotted alongside experimental results for wall shear stress measurements in the 2.0” conduit. Note that the experimental data differs by an order of magnitude from the experimental data.	78
Figure 27. Plot of bottom wall shear stress as a function of position across the conduit for Isopar-V produced by CFD simulations.	79
Figure 28. Plot of wall shear stress (Pa) as a function of top plate rotational speed (RPM). Data was acquired using a different wall shear stress probe of the same specifications as the probe used in all other wall shear stress experiments.	82
Figure 29. Cross section of the annular flume showing gap between top plate and outer wall (Al Schubert of the ICMT).	83
Figure 30. Phase wetting map of proprietary crude oil.	85
Figure 31. Phase wetting map of LVT-200 V.....	86
Figure 32. Phase wetting map of Isopar-V.	86
Figure 33. Plots of top friction factors and bottom friction factors as functions of Reynolds number on a logarithmic scale.	88
Figure 34. Plots of vertical velocity for LVT-200 and Isopar-V at 163.4 RPM.	100

GLOSSARY

β	Pipeline inclination [degree]
C_H	Brauner constant
d_{32}	Mean droplet diameter [m]
D_h	Hydraulic diameter [m]
d_{max}	Maximum droplet diameter [m]
$d_{max,o}$	Maximum droplet diameter in dilute dispersions, m
d_{crit}	Critical droplet diameter [m]
d_{cb}	Critical droplet diameter due to gravity effect [m]
$d_{c\sigma}$	Critical droplet diameter due to droplet deformation [m]
D	Pipe diameter [m]
ϵ_w	Water-cut [%]
ϵ	Mean energy dissipation rate [W/kg]
f	Friction factor
f_{Top}	Top plate Fanning friction factor
f_{Bottom}	Bottom plate Fanning friction factor
$f_{Bottom\ exp}$	Experimental bottom plate Fanning friction factor
f_T	Turbulent force [N]
f_G	Gravitational force [N]
IP	Inversion point [%]
ω	Angular velocity of top plate [rad/sec]
R_m	Mid-radius of annular flume conduit [m]
R_I	Inner wall radius [m]
R_O	Outer wall radius [m]
ρ_c	Density of the continuous phase (oil phase) $\left[\frac{\text{kg}}{\text{m}^3}\right]$
ρ_d	Density of the dispersed phase (water phase) $\left[\frac{\text{kg}}{\text{m}^3}\right]$
ρ_m	Density of the mixture (oil and water) $\left[\frac{\text{kg}}{\text{m}^3}\right]$

σ	Oil/water interfacial tension $\left[\frac{\text{N}}{\text{m}}\right]$
τ	Wall shear stress [Pa]
τ_{WT}	Top plate wall shear stress [Pa]
τ_{WB}	Bottom plate wall shear stress [Pa]
τ_{WO}	Outer wall shear stress [Pa]
τ_{WI}	Inner wall shear stress [Pa]
τ_{WBexp}	Experimental bottom plate wall shear stress [Pa]
T_{Total}	Total torque in annular flume [N m]
T_T	Top plate torque [N m]
T_B	Bottom plate torque [N m]
T_O	Outer wall torque [N m]
T_I	Inner wall torque [N m]
U_c	Velocity of the continuous phase (oil phase) [m/s]
U_T	Tangential speed of rotating top plate [m/s]
μ_c	Viscosity of continuous phase [Pa.s]
u'	Friction Velocity [m/s]

INTRODUCTION

One of the largest problems in the transportation of oil through carbon steel pipelines is corrosion. From 1999 to 2001, the U.S. Federal Highway Administration (FHWA) performed a study to determine the costs of damage resulting from metallic corrosion in every major U.S. industry sector. The total cost was estimated to be approximately \$276 billion, which is nearly 3.1% of the nation's Gross Domestic Product (GDP) (Koch, Bongers, *et al.*, 2002). Of this, approximately \$5.6 billion is directly attributed to damage resulting from the transmission of oil and other fluids through pipelines by oil companies. More recently, NACE estimated the annual cost of corrosion to be approximately \$2.5 trillion, globally; however, it is estimated that approximately 35% of this cost could be deferred using corrosion control measures (NACE, 2016).

There are a number of ways to mitigate metallic corrosion, including the use of polymeric coatings on the internal surface of the pipeline, or through the use of corrosive resistant alloys (CRA's). Unfortunately, given that there are more than 74,000 miles of oil and liquid transmission pipelines in the U.S. alone (Koch, *et al.*, 2002), as well as the high cost of polymeric coatings and CRA's, the cost of replacing the current carbon steel pipelines would be impractical. Instead, carbon steel has been prevalently used due to its durability, low cost, and ease of manufacturing.

Gaseous CO₂ and water are naturally occurring in most oil wells, and are subsequently pumped along with oil within pipelines. When CO₂ dissolves in water, it forms carbonic acid, which reacts with the carbon steel pipeline, resulting in corrosion (Nesic *et al.*, 2003). This occurs when the water phase is in contact with the steel surface

leading to a phenomenon called water wetting. In two-phase oil-water flow, water wetting occurs when the water phase and the oil phase flow in a stratified manner. When the volumetric fraction of water within the pipeline (water cut) is sufficiently low and the flow velocity is sufficiently high, this is not an issue, as the flow is sufficiently turbulent to entrain the water phase within the oil phase. When the water phase is entrained within the oil phase, the water phase does not meet the steel surface, but the oil phase does. When the walls of the pipeline are wetted with oil, no corrosion is possible (Cai et al., 2005). It is for this reason that entrainment of the water phase, and water wetting, in general, are of major interest. Certain parameters play an important role in preventing water wetting, including flow velocity, water properties, oil composition, among others. Developing an understanding of these factors is crucial in preventing CO₂ corrosion of internal pipelines. Numerous models based upon these factors have been developed with the aim of predicting phase wetting, the dispersion of one fluid phase (dispersed phase) into another fluid phase (continuous phase).

In 2012, the Institute for Corrosion and Multiphase Technology (ICMT) developed a water wetting model based on an approach proposed by Cai (Cai et al., 2012). This model has since been updated by Paolinelli (Paolinelli et al., 2018). The model, used to predict the transition between dispersed and stratified flow, has been validated, albeit in a limited way, using experimental data collected from a 4 in. ID, 40m flow loop located within the ICMT facility. This flow loop provides an environment where two phase oil/water flow can be controlled and monitored. Data can be acquired within a test section made of a type carbon steel similar to the ones used in oil and gas

pipelines across the world. Oil and water are both pumped from separate 250 gallon tanks through the entire loop at an adjustable velocity. Phase wetting data is acquired using wall conductance probes that are flush mounted to the lower circumference of the test section. These probes can identify which fluid phase is wetting the carbon steel surface by measuring the conductivity of the fluid (salt containing water (brine) displays high conductivity while oil shows very low conductivity).

Due to the size of the flow loop, experimentation requires extensive time, manpower, and volumes of oil. In order to make experimentation more timely and efficient, a small-scale apparatus, called the annular flume apparatus, was developed. Two phase oil/water flow is induced in an annular channel formed by an inner cylinder and an outer cylinder made of stainless steel, respectively. The bottom plate of the annular cavity is made of stainless steel. It is capable of acquiring data on velocity, wall shear stress, and phase wetting, much like the flow loop. However, difficulties were encountered to relate the data collected on velocity and wall shear stress between the two experimental systems; i.e. flow loop and annular flume. It is unclear whether this annular flume apparatus provides an accurate representation of pipeline flow; more specifically, it is unclear whether data acquired by the annular flume can be scaled up to model pipeline flow. In order to determine this, CFD simulations of multiphase flow must be performed; however the first step towards modeling multiphase flow is modeling single phase flow. The main goal of the present work is to perform CFD simulations of single phase flow and validate them with experimental measurements of tangential velocity (m/s) and wall shear stress (Pa) to characterize the hydrodynamics of the annular flume. The CFD

simulations were eventually used to modify a key parameter of the water wetting model to better suit the flow characteristics of the annular flume. Additionally, phase wetting data was collected in two phase oil/water flow .

BACKGROUND

2.1. Water Wetting Fundamentals

The background section will discuss the fundamentals of two phase oil/water flow, and present previous studies used in the development of the water wetting model currently in use at the Institute for Corrosion and Multiphase Technology.

Water wetting of the steel surface in two-phase oil/water pipe flow is heavily dependent on the type of flow regime within the pipeline. The term flow regime refers to the type of arrangement formed by the water phase and oil phase while flowing through the pipeline. There are two main categories of flow regimes in horizontal oil-water flow: stratified flow and dispersed flow. Stratified flow occurs when the water phase and the oil phase are completely stratified, as shown in Figure 1. This flow regime is when water wetting and subsequent corrosion of the pipe occurs.

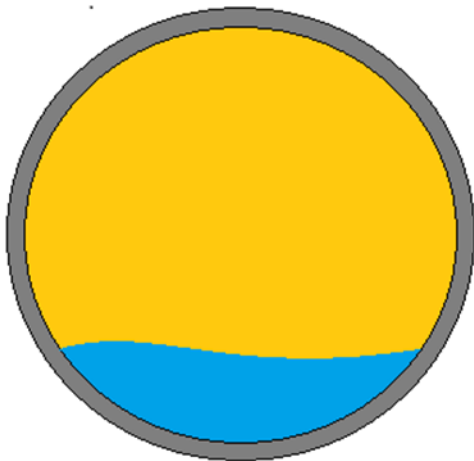


Figure 1. Diagram of stratified flow in two phase oil-water pipe flow, wherein water (blue), and oil (yellow) flow in segregated layers.

Dispersed flow, shown in Figure 2, is the desired type of flow to be achieved within oil pipelines. Because the water phase, the dispersed phase, is entrained within the oil phase, the continuous phase, oil wetting occurs at the steel surface; therefore, there is no water wetting, and, subsequently, no corrosion. Many water wetting models have been developed that aim to predict the transition from dispersed flow patterns.

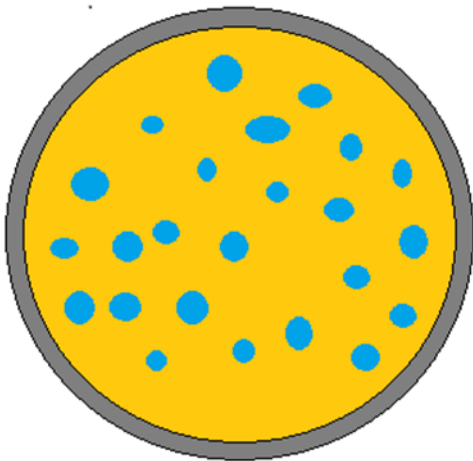


Figure 2. Diagram of dispersed flow in two phase oil-water pipe flow wherein the water phase (blue) is fully dispersed in droplets entrained by the oil phase (yellow).

2.2. Predicting the Transition from Dispersed Flow

Much of the work done on predicting the transition from dispersed flow to stratified flow is done based upon the work of Brauner (Brauner, 2001) and Hinze (Hinze, 1955). Water wetting models are designed to predict the transition from dispersed flow to stratified flow in two-phase oil-water pipe flow. These models assume that the stability of dispersed flow is based upon a balance of turbulent forces from continuous phase flow, F_T , and gravitational force, F_g , on the dispersed phase droplets, as shown in Figure 3. The

magnitude of the turbulent forces increases with increasing continuous phase velocity. At a critical continuous phase velocity, $F_T \geq F_g$, and the magnitude of turbulent forces is sufficient to entrain dispersed phase droplets, resulting in a dispersed flow regime. At flow velocities below the critical continuous phase velocity, $F_T < F_g$, and turbulent forces are not sufficient to entrain dispersed phase droplets, resulting in a stratified flow regime.

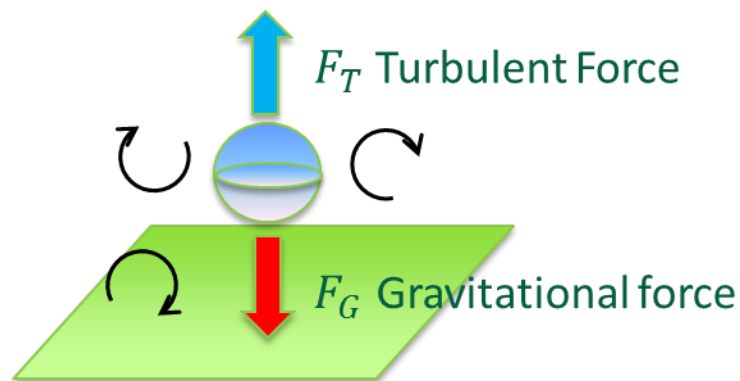


Figure 3. Diagram of turbulent force, F_T , and gravitational force, F_G , acting on a dispersed phase droplet.

There are additional factors that contribute to the prediction of the transition from dispersed flow in two phase liquid-liquid flow in horizontal pipes. Water wetting models have incorporated the effect of the volumetric fraction of water (water cut), pipe diameter, fluid flow rates, and fluid properties, including density, interfacial tension and viscosity in the prediction of phase wetting (Wicks and Fraser, 1975; Smith et al., 1987; Adams et al., 1993; Cai et al., 2005; Cai et al, 2012). It was originally assumed by many investigators that the critical velocity required for dispersed flow depended solely upon the volume fraction of water within the pipeline (water cut). Previous studies provided

crude criteria to obtain the critical velocity. Works from Wicks and Fraser (Wicks and Fraiser, 1975), Smith et al. (Smith et al., 1987), and Adams et al. (Adams et al., 1993) were among some of these previous studies that focused solely on water cut. That is, they assumed the sole factors affecting water entrainment were flow velocity and water cut, while they neglected factors like water chemistry, crude oil chemistry, system temperature, and pipe diameter, amongst other factors. This approach led to studies such as that of Smith et al. (Smith et al., 1987) that concluded that oil has the ability to entrain water with up to 20% water cut if flowing at velocities larger than 1 m/s; however, Cai et al. (Cai et al., 2012), have provided evidence of water wetting still occurring within these constraints.

C. de Waard et al. (de Waard, 2001; de Waard, 2003) proposed an improved model based on the emulsion breakpoint. That is, they consider the effect of interfacial tension on emulsion stability and water wetting of the internal steel surface of the pipeline. Nevertheless, most of these studies failed to accurately predict the transition to dispersed flow observed experimentally, especially at higher water cuts (Cai et al., 2012).

Cai et al. (Cai et al., 2005) improved modeling of water wetting by including the effect of pipe diameter and pipe inclination. This model assumes as a starting point that the water phase is already entrained within the oil phase and evaluates the conditions necessary to maintain water entrainment. This model assumes that the sole action of the turbulent kinetic energy of the oil phase is to keep already existing water droplets entrained within the oil phase from coalescing, rather than to create and lift water droplets from the stratified water layer. In other words, the transition from dispersed flow

to stratified flow is considered rather than the opposite. This model accounts for the change in oil-water interfacial energy; however, it neglects other interactions with the pipeline surface. In assuming that the water phase is already entrained in the oil phase, this model neglects any change in the water-steel or oil-steel surface energy (Cai et al., 2012). This represents a fundamental but only preliminary step in understanding water wetting. In other words, the transition from dispersed flow to stratified flow must be understood before the more complex problem of including surface energies in the transition from stratified flow to dispersed flow can be solved.

The surface wettability (i.e. hydrophobic or hydrophilic) of the pipe surface was shown to affect the transition boundaries of phase wetting regimes and the transition to fully dispersed flow in both horizontal pipe flow (Paolinelli et al., 2018) and annular flume flow (Gardner, 2017). Hydrophilic surfaces, such as carbon steel, result in increased critical flow velocities sufficient for full entrainment of water in oil as compared to those critical flow velocities observed on hydrophobic surfaces. This is due to the differing inherent mechanisms that are responsible for segregation of water layers and subsequent water wetting for differing pipe surface wettability. A hydrophilic surface wettability will favor the deposition and spreading of water droplets on the pipe surface, leading to the formation of water streams, segregation of water layers from oil layers.

Alternatively, a hydrophobic surface, such as stainless steel, inhibits to some extent the deposition and spreading of water droplets. In this instance, segregation of water layers requires a sufficiently low flow velocity to enable droplet accumulation and coalescence near the bottom surface.

Moreover, a metastable surface wettability is observed on carbon steel surfaces depending upon the phase, water or oil, which wets the surface first (Paolinelli et al., 2018). A hydrophobic surface wettability is observed if the surface is initially oil wet; whereas a hydrophilic surface wettability is observed if the surface is initially water wet.

2.3. ICMT Water Wetting Model

The current water wetting model developed by the Institute for Corrosion and Multiphase Testing (ICMT) is based on the works of Hinze (Hinze, 1955) and Brauner (Brauner, 2001). Its predictions agreed well with experimental results in horizontal pipe flow with surfaces of varied wettability (Paolinelli et al., 2018). In the future, this model will be adapted to the annular flume through the modeling of multiphase flow, thus enabling for the prediction of phase wetting regimes in two phase oil-water flow. The model assesses the stability of fully dispersed water in oil flow and is as follows.

Droplet diameter, d , is assumed to be the result of droplet breakup due to turbulent eddies (Hinze, 1955). In this manner, the maximum diameter of the turbulent eddies determines the maximum diameter of the dispersed phase droplets, d_{max} . This is depicted in Figure 4.

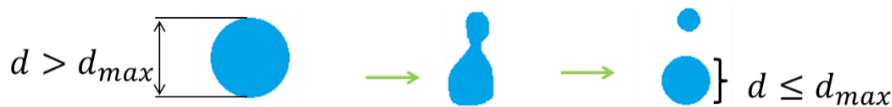


Figure 4. Depiction of turbulent breakup of dispersed phase droplets (Yao, 2016).

Because the maximum diameter of the turbulent eddies is determined by the energy dissipation rate of the continuous phase, the maximum droplet size in turbulent flow in

pipes of diameter, D (m), is a function of the mean energy dissipation rate of the continuous phase, ϵ (Hinze, 1955).

$$\epsilon = \frac{4\tau U_c}{D\rho_c(1 - \epsilon_d)} = \frac{2\rho_m f U_c^3}{D\rho_c(1 - \epsilon_d)} \quad (1)$$

where τ = wall shear stress, Pa

U_c = flow velocity of continuous phase, $\frac{m}{s}$

ϵ_d = volume fraction of water (water cut) (dimensionless)

f = friction factor (dimensionless)

ρ_m = mixture density, $\frac{kg}{m^3}$

ρ_c = continuous phase density, $\frac{kg}{m^3}$

In dilute dispersions, the maximum droplet size is obtained using Hinze's approach (Hinze, 1955),

$$d_{max,o} \cong C_o \left(\frac{\sigma}{\rho_c} \right)^{\frac{3}{5}} \epsilon^{-\frac{2}{5}} \quad (2)$$

Where $d_{max,o}$ = maximum droplet diameter in dilute dispersions, m

ρ_c = density of continuous phase, $\frac{kg}{m^3}$

σ = oil-water surface tension, $\frac{N}{m}$

ϵ = mean energy dissipation rate in the continuous phase, $\frac{W}{kg}$

The value of the constant, C_o , in equation (2) was determined experimentally to be 1.39 (Paolinelli et al., 2018).

This equation is valid provided it agrees with the following criteria (Brauner, 2001).

$$\left(\frac{\mu_c^3 \epsilon}{\rho_c^3}\right)^{\frac{1}{4}} \ll d_{max,o} < 0.1D \quad (3)$$

Where μ_c = the continuous phase viscosity, Pa s.

The maximum droplet diameter increases with increasing volumetric fraction of the dispersed phase. To account for this, the following equation is used (Mlynek & Resbick, 1972).

$$d_{max} = d_{max,o}(1 + 5.4\epsilon_d) \quad (4)$$

The mean droplet size, d_{32} , is proportional to the maximum droplet size, as shown in the following equation.

$$d_{32} = C_m d_{max} \quad (5)$$

Where C_m was found to be 0.49 (Paolinelli et al., 2018).

The stability of fully dispersed flow is evaluated using criteria developed in previous models. These models assume that the flow is already fully dispersed. Brauner's model proposed that the rate of turbulent energy of the continuous phase should balance the rate of surface energy creation (droplet coalescence) in the dispersed phase, forming droplets smaller than the critical droplet diameter for dispersion, d_{crit} with the following criterion for dispersed water in oil:

$$d_{max} < d_{crit} \quad (6)$$

With the criteria, $Re_c \geq 2100$, where $Re_c = \frac{\rho_c D U_c}{\mu_c}$.

The critical diameter determined by the following equation.

$$d_{crit} = \text{Min}(d_{c\sigma}, d_{cb}). \quad (7)$$

where $d_{c\sigma}$ is the maximum diameter globules can reach before they will undergo deformation, and d_{cb} is the maximum diameter globules can reach before buoyant forces cause diffusion towards the pipeline walls (Brodkey, 1969). These variables are defined as follows,

$$d_{cb} = \frac{3}{8} \frac{\rho_c}{|\rho_d - \rho_c|} \frac{fU_c^2}{g \cos \beta} \quad (8)$$

Where g is the gravitational acceleration, and β is the inclination angle of the pipe. The following arises from a ratio between the turbulent flow force applied to the droplet and the gravity force in the radial direction of the pipe (Paolinelli et al., 2018).

$$d_{c\sigma} = \left[\frac{0.4\sigma}{|\rho_d - \rho_c| g \cos \beta'} \right]^{1/2} \quad (9)$$

Where β' (rad) is mathematically related to the inclination angle of pipe β :

$$\beta' = \begin{cases} |\beta|, & |\beta| < 45^\circ \\ 90 - |\beta|, & |\beta| > 45^\circ \end{cases}$$

The constants used in $d_{c\sigma}$, 0.4, was determined using experimental data from a particular system, and should be modified for experimental data for a different system (Brauner, 2001).

The Fanning friction factor for pipe flow, f , is estimated using the Blasius type correlation (Paolinelli et al., 2018):

$$f = 0.046 Re_m^{-0.2} \quad (10)$$

Where $Re_m = \frac{\rho_m D U_m}{\mu_m}$, the mixture viscosity, U_m , is estimated as being approximately equal to the continuous phase, ($U_m \cong U_c$), and the density of the oil-water mixture is determined by the following equation (Elseth, 2001):

$$\rho_m = \varepsilon_d \rho_d + (1 - \varepsilon_d) \rho_c \quad (11)$$

The present study aims to determine Fanning friction factors in the configuration of the annular flume. In the case of hydrophobic, non-adherent interior pipe surfaces, dispersed droplets are unlikely to stick to the pipe wall and spread, forming a segregated water stream (Pots et al., 2006). These droplets would subsequently be re-entrained by the continuous boundary layer, continuing fully dispersed flow regime. The previous criteria would subsequently over-predict (not be valid in predicting phase wetting in this scenario) phase wetting without accounting for this mechanism behind phase wetting (Paolinelli et al., 2018). Accumulation and concentration of droplets at the pipe bottom must be accounted for.

The water droplet concentration at the pipe bottom, C_b , must be large enough to reach a critical concentration in which droplets become unstable, coalesce, and form a segregated layer of water. A water stream would form at a concentration approximately equal to the phase inversion point (IP), the volumetric fraction of water above which a dispersion of water in oil will invert to a dispersion of oil in water. Preventing the accumulation and coalescence of droplets at the pipe bottom thus requires the following criterion:

$$C_b < IP \quad (12)$$

An advection diffusion equation is used to approximate the droplet concentration on a cross section of pipe (Karabelas, 1977). This is equation assumes steady state conditions in horizontal flow and accounts for the mass balance of the dispersed droplets and the fluxes of the continuous phase:

$$U_s C(1 - C) - \varepsilon \frac{\partial C}{\partial y} = 0 \quad (13)$$

Where C is the droplet volumetric concentration, ε is the turbulent diffusivity with the assumption that it is constant across the pipe section, and is determined by the following equation:

$$\varepsilon = \zeta \frac{D}{2} \sqrt{\frac{\rho_m f}{2\rho_c}} U_m \quad (14)$$

Where ζ is the dimensionless eddy diffusivity which is approximated as a constant of 0.255 (Karabelas, 1977). U_s is the settling velocity of the mean droplet size:

$$U_s = \sqrt{\frac{4}{3} \frac{d_{32} |\rho_d - \rho_c| g}{\rho_c C_D}} \quad (15)$$

Where C_D is the droplet drag coefficient, approximated by the following Schiller-Naumann correlation for solid spheres (Schiller and Naumann, 1933):

$$C_D = \frac{24}{Re_p} (1 + 0.15 Re_p^{0.687}) \quad (16)$$

where $Re_p = \frac{\rho_c d_{32} U_s}{\mu_c}$ for $Re_p < 1000$.

The advection-diffusion equation for droplet accumulation, equation (13), does not account for the effect of hydrodynamic forces near the wall. In this instance, droplet

concentration only varies in the vertical, y-direction of the pipe ($C(y)$), and the cumulative droplet mass is constant across the pipe section ($\int C(y)dA = \varepsilon_d A$). That is, droplets do not stick to the pipe interior, nor do droplet sizes vary with time.

The closed form solution of equation (13) yields the approximation of the droplet concentration at the pipe bottom (Karabelas, 1977).

$$C_b = \left[1 + 2 \frac{1 - \varepsilon_d}{\varepsilon_d} \frac{I_1(K)}{K} \exp(-K) \right]^{-1} \quad (17)$$

Where

$$K = \frac{DU_s}{2\varepsilon} \quad (18)$$

and I_1 is the modified Bessel function of order 1:

$$I_1(K) = \frac{1}{2}K \left[1 + \frac{K^2}{8} + \frac{K^4}{192} + \frac{K^6}{9216} + \frac{K^8}{737280} + \frac{K^{10}}{88473600} \right] \quad (19)$$

This series approximates the modified Bessel function for K values as high as 4, which only overestimates droplet concentrations less than 10% in conjunction with equation (17) (Paolinelli et al., 2018).

This criterion was shown to provide a good prediction of the transition from fully dispersed flow over a range of experimental data for a hydrophobic PVC pipe (Paolinelli et al., 2018). Thus, the hypothesis of hydrophobic surfaces inhibiting the sticking and spreading of water droplets was confirmed. The main mechanism of action for segregation of water layers is the formation of the critical concentration of water droplets at the pipe bottom similar to the phase inversion point, subsequently forming a water stream.

Additionally, the criteria showed good predictions of the transition from fully dispersed flow in hydrophilic pipes. The transition to fully dispersed flow and oil wet regime of the pipe internal surface results from significantly higher mixture velocities in hydrophilic pipes in comparison with hydrophobic pipes.

Much of the research on liquid-liquid flow in pipes was conducted on large scale flow loops. Due to their size, these flow loops require extensive amounts of time, hydrocarbon fluid, man power, cleaning of equipment (pumps, pipes, separators, dispersed phase coalescers, etc.), and cleaning supplies. This makes testing with large scale flow loops to be unfavorable for collecting data, especially in comparison to a small scale apparatus capable of reproducing this type of fluid flow testing.

2.4. Flow Characteristics in Annular Flume Apparatus

The apparatus proposed in the present study comprises a rectangular annular flume formed by inner and outer stainless steel cylinders, a stainless steel bottom plate, and rotating top plate that induces shear driven flow similar to Couette flow, see Figure 5. Studies on similar apparatuses have been performed to determine whether the apparatus would give an accurate representation of pipeline flow in the prediction of phase wetting. de Dood (de Dood, 1997) performed computational fluid dynamic simulations and experimental measurements to characterize the hydrodynamics of the flow. A significant secondary cross flow was observed which is uncharacteristic of pipeline flow. A secondary flow was predicted to form due to the cylindrical geometry of the conduit, and the method of flow induction by shear from a rotating top plate (Yang et al., 2000).

Because the water wetting model described in the previous section is exclusive to horizontal pipe flow, modifications must be made to a key parameter (Fanning friction factor) in order to predict the onset of fully dispersed flow and oil wet regime in the annular flume presented in this study. This is due to key differences between annular flume flow and pipe flow. Pipe flow is pressure driven and annular flume flow is shear driven by a rotating top plate.

In order to adapt the input parameters of the water wetting model, the hydrodynamics of flow in the annular flume presented in this study must be properly characterized. To date, there has not been any comprehensive effort to characterize the flow the annular flume presented in this study, which is a necessary step prior to any interpretation of the collected data. Numerical modeling of multiphase flow in the annular flume is required for comprehension of the flow characteristics. The first step towards numerical modeling multiphase flow is numerical modeling of single phase flow.

The model results of single phase flow in the present study were used to produce two separate Blasius type correlations of Fanning friction factors corresponding to the top plate, f_{Top} , and bottom plate, f_{Bottom} , of the annular flume, respectively. Experimental results of bottom wall shear stress can also be used to determine a Blasius type correlation for an experimental bottom plate Fanning friction factor, $f_{Bottom\ exp}$, similarly to f_{Bottom} .

The Blasius type correlations are described as follows.

$$f_{Top} = C_1 Re^{C_2} \quad (20)$$

$$f_{Bottom} = C_3 Re^{C_4} \quad (21)$$

$$f_{Bottom\ exp} = C_5 Re^{C_6} \quad (22)$$

Where the constants C_1, C_2, C_3, C_4, C_5 , and C_6 were determined once the Fanning friction factors are plotted as a function of Reynolds number. C_1, C_2, C_3, C_4 are determined through fitting with modeling results while C_5 , and C_6 are obtained through fitting with experimental data. These Blasius type correlations allow future calculations of the Fanning friction factors using fluid properties and top plate tangential velocity, U_T , without requiring results from CFD simulations.

Separate Fanning friction factors were determined for the annular flume and it is important to clearly explain the meaning of these two parameters and how they are used within the water wetting model. In the annular flume, friction factors arise from the presence of shear stresses generated by the motion of the top plate.

The total torque, T_{Total} , associated with the circular motion of the top plate in the annular flume can be written as follows (Gardner, 2017).

$$T_{Total} = T_T = T_B + T_I + T_O \quad (23)$$

Where T_T is the torque at the top plate, T_B is the torque at the bottom plate, T_I is the torque at the inner wall, and T_O is the torque at the outer wall.

The torque at the top plate can be further described as follows (Gardner, 2017).

$$T_T = \int r \times \tau_{WT}(r) dA = \int r \times \tau_{WB}(r) dA + \int r \times \tau_{WO}(z) dA + \int r \times \tau_{WI}(z) dA \quad (24)$$

Where $\tau_{WT}(r)$ is the shear stress at the rotating top wall, $\tau_{WB}(r)$ is the shear stress at the bottom wall, and $\tau_{WO}(z)$ and $\tau_{WI}(z)$ are the shear stresses at the outer and the inner walls, respectively.

As T_I and T_O are both non-zero, the equation for torque in the annular flume shows that $T_B < T_T$. That is, $\tau_{WB}(r) < \tau_{WT}(r)$. Pipe flow does not exhibit this type of hydrodynamic characteristic because pipe flow is pressure driven; whereas annular flume flow is shear driven by a rotating top plate.

As outlined in section 2.3, the ICMT water wetting model that has been determined for pipe flow has one Fanning friction factor used as part of the calculation for the mean energy dissipation rate (ϵ), equation (1), and the critical droplet diameter (d_{cb}), equation (8). As shown by the following equation, the Fanning friction factor for a pipe configuration is a function of the wall shear stress, τ , defined by the following equation.

$$f = 2 \frac{\tau}{U_c^2 \rho_c} \quad (25)$$

Where pipe flow requires only one Fanning friction factor, as it is done for ICMT water wetting model, the full characterization of the flow in the annular flume requires two separate Fanning friction factors for the top plate and bottom plates, respectively. As part of a conservative approach to predicting water wetting in the annular flume apparatus, the Fanning friction factor corresponding to the top of the annular flume, f_{Top} , is intended primarily used to calculate the mean energy dissipation rate ϵ , and consequently the maximum diameter of the dispersed phase droplets, d_{max} , for initial

predictions of water wetting. The Fanning friction factor corresponding to the bottom of the annular flume, f_{Bottom} , is used to determine the critical droplet diameter, d_{cb} .

The maximum droplet size, d_{max} , depends on the mean energy dissipation rate ϵ which is directly related to the average torque of the top plate, and consequently to f_{Top} . Since the torque is averaged over the entire top plate, the expression of f_{Top} also corresponds also an average value. Minimum values of d_{max} in the annular flume are expected to occur at the top plate, where magnitudes of wall shear stress and turbulence are at maximum values, according to equation (2). Using a minimal value of d_{max} in the criteria for evaluating the stability of dispersed flow, defined by equation (6), is more conservative than using larger values of d_{max} that are expected to occur closer to the bottom plate where values of torque and turbulence are lower than values of torque and turbulence near the top plate. In this manner, the calculation of ϵ using f_{Top} , even though it is averaged over the entire top plate, provides for an initial, rather conservative, step in the prediction of phase wetting in the annular flume. More accurate values of d_{max} close to the bottom plate may be obtained using the bottom wall shear stress, leading to a less conservative evaluation of the stability of dispersed flow and subsequent prediction of phase wetting. However, at this stage of the study, a more conservative approach is preferred.

The power input of the annular flume is transferred to the fluid by means of the rotating top plate. Since all of the power input in shear driven flow is dissipated or transformed into turbulence and then heat, it is equivalent to the mean energy dissipation rate. The torque and the rotational speed of the rotating top plate can be used to determine

the power input of the rotating top plate into the fluid annular flume. This power input, or mean energy dissipation rate, of the annular flume is described as follows.

$$\epsilon = \frac{T_T \omega}{D \rho_c (1 - \epsilon_d)} \quad (26)$$

Where T_T (N m) is the torque of the rotating top plate, and ω is the angular velocity of the rotating top plate (rad/sec). The top plate torque T_T , or $\int r \times \tau_{WT}(r) dA$, can be estimated for future calculations once the top Fanning friction factor is known.

Because torque decreases towards the bottom of the annular flume conduit, droplets are expected to fall from entrainment due to insufficient suspension forces near the bottom of the conduit where torque would be at a minimum. Since it is related to T_B , the bottom Fanning friction factor, f_{Bottom} , is used directly in the calculation of the critical droplet diameter, d_{cb} . The following equation for d_{cb} has been modified from equation (8) to suit the annular flume.

$$d_{cb} = \frac{3}{8} \frac{\rho_c}{|\rho_d - \rho_c|} \frac{f_{Bottom} U_T^2}{g} \quad (27)$$

Where U_T ($\frac{m}{s}$) is defined as follows.

$$U_T = \omega R_m \quad (28)$$

Where R_m (m), the mean radius of the rotating top plate, is defined as follows.

$$R_m = \frac{R_o + R_i}{2} \quad (29)$$

A depiction of these dimensions is shown in Figure 5. The CFD results can be used to generate expressions of f_{Top} and f_{Bottom} as a function of Reynolds number. The

CFD generated values for torque, T_T and T_B , are integrated across the area of the top plate and bottom plate, respectively. These values are then used to determine τ_{WT} and τ_{WB} , respectively. The equations to calculate τ_{WT} and τ_{WB} are as follows.

$$\tau_{WT} = \frac{3}{2} \frac{T_T}{\pi(R_O^3 - R_I^3)} \quad (30)$$

$$\tau_{WB} = \frac{3}{2} \frac{T_B}{\pi(R_O^3 - R_I^3)} \quad (31)$$

Where R_O (m) is the radius of the outer wall of the channel and R_I is the radius of the inner wall of the channel.

Finally, the top plate wall shear stress, τ_{WT} , and the bottom wall shear stress, τ_{WB} , are used to determine f_{Top} and f_{Bottom} as follows.

$$f_{Top} = 2 \frac{\tau_{WT}}{\rho_c U_T^2} \quad (32)$$

$$f_{Bottom} = 2 \frac{\tau_{WB}}{\rho_c U_T^2} \quad (33)$$

The experimental results of bottom wall shear stress, τ_{WBexp} , obtained from hydrodynamic study of experimental bottom wall shear stress results in section 7.5, were used to calculate $f_{Bottom exp}$ as follows.

$$f_{Bottom exp} = 2 \frac{\tau_{WBexp}}{\rho_c U_T^2} \quad (34)$$

The Fanning friction factors for varying data points must be plotted as a function of the Reynolds number, defined as follows.

$$R_e = \frac{\rho D_h U_T}{\mu_c} \quad (35)$$

where the hydraulic diameter, D_h (m), is defined by

$$D_h = \frac{4 \times Area}{Wetted Perimeter} = \frac{4H(R_o - R_i)}{2H + (R_o - R_i)} \quad (36)$$

Where H (m) is the height of the annular flume.

Due to the top plate being the means of flow induction and constantly rotating, the annular flume conduit is being treated as an open channel; hence the surface of the top plate is not accounted for in the wetted perimeter.

PROJECT OBJECTIVES

The water wetting characteristics of crude oil/water flow still requires calibration with experimental data due to the complex formulation of crude oils. Without this calibration, no model, even the most mechanistic one, will be able to accurately predict phase wetting. These data are typically obtained through expensive and cumbersome flow loop experiments. The smaller scale setup of the annular flume apparatus has been proposed to address these issues and enable rapid data collection and characterization. However, there has not been any comprehensive effort to characterize the flow in this annular flume apparatus, which is a necessary step prior to any interpretation of the collected data.

Numerical modeling of multiphase flow in the annular flume is required for full comprehension of the flow characteristics. The first step of this process is numerical modeling of single phase flow. Therefore, it was the aim of this research work to hydrodynamically characterize single phase flow in the annular flume by performing numerical simulations using computational fluid dynamics and verifying the results of these numerical simulations with experimental measurements of hydrodynamic parameters of single phase flow in an overall effort to build correlations with pipeline flow. These experimental hydrodynamic parameters include wall shear stress (Pa) and tangential velocity (m/s). The results of the CFD simulations were used to modify a Fanning friction factor, a key parameter in the ICMT water wetting model, to suit annular flume flow. Specifically, two Fanning friction factors were determined: one corresponding to the top of the conduit in the annular flume, and one corresponding to the

bottom of the conduit. The top Fanning friction factor can be used to determine the turbulent energy dissipation rate, while the bottom Fanning friction factor can be used to determine droplet properties close to the bottom plate of the annular flume. We hypothesize that the results from numerical simulations of single phase flow will be verified by experimental hydrodynamic measurements, and proper Fanning friction factors will be determined. Experiments on phase wetting were performed to observe phase wetting behavior in the annular flume.

SCOPE OF WORK AND TEST MATRICES

This section presents a summary of the range of operating conditions and a brief description of the test setups and measurement techniques that are selected to collect the experimental data. The type of CFD modeling approach, used to characterize the hydrodynamics of the flow in the annular flume, is also briefly discussed. Finally, the experimental matrices are proposed.

4.1. Scope of Work

4.1.1. Range of Fluid Properties Used in the Study

The hydrodynamics parameters of the annular flume flow are collected in single-phase flow using fluids (water and two model oils) with physical properties covering a wide range of conditions. The phase wetting study is performed considering a two-phase oil/water system. The oil phases used in this study are LVT-200, Isopar-V, and a proprietary crude oil. It is necessary to use model oils because their compositions are known, and they contain no volatile constituents that may affect experimental results. They were chosen because of their differing viscosities and interfacial tensions, which provide a broader range of results. Their properties are shown in table 1. The aqueous phase is DI water + 1 wt% NaCl (salt is added to facilitate some of the measurement of conductivity), referred to as brine throughout the remainder of the document.

Experiments are conducted at a constant atmospheric pressure and temperature.

Table 1.

Fluid properties (model oils and water) used in experimentation.

Properties at 25°C and 1.01 bar	LVT-200	Isopar-V	1% wt. NaCl Brine	Prop. Crude Oil
ρ (kg/m ³)	825	813	1196	870
μ (cP)	2.7	13.3	1.3	8.7
σ (mN/m)	47.0	27.1		20.7

4.1.2. Scope of the Hydrodynamic Study

The annular flume is used to conduct measurements on hydrodynamic parameters. Specifically, pitot tubes fitted with differential pressure transducers and digital transducer readers are used to measure in situ circumferential velocity of the oil phase, and a wall shear stress probe flush mounted to the bottom plate of the annular flume is used to conduct wall shear stress (WSS) measurements. These measurements are compared with CFD simulations to validate the turbulence model. Additionally, experimental flow data from the hydrodynamic study are used to generate experimental expression of the Fanning friction factor, which are later compared to modeling results.

4.1.3. Scope of Phase Wetting Study

Characterization of phase wetting regimes in two phase oil/water flow is conducted using varying water cuts at two different channel diameters. Conductance

probes, flush-mounted to the bottom surface of the annular conduit, are used to determine phase wetting regimes. They can determine which phase, oil or water, is wetting the bottom surface due to the electrical conductance of water and the non-conductance of oil.

4.1.4. Scope of Numerical Modeling

Experimental data from the annular flume will be used to verify the turbulence model, the $k - \varepsilon$ turbulence model used in the single phase CFD simulations. This turbulence model is described in Appendix 1. Experimental data will be compared with model results to validate the turbulence model in terms of the hydrodynamic conditions within the annular flume. Flow data from the simulations will be used to modify a key parameter of the water wetting model, the Fanning friction factor.

4.2. Test Matrices

The test matrix for single phase hydrodynamic experiments is shown in table 2. The test matrix for phase wetting experiments is shown in table 3. Single phase experiments wherein hydrodynamic measurements are taken are conducted in two channel heights: 2.0 inch. and 4.5 inch. This allows observations to be made on the effect of varying the diameter of the channel as this is an important parameter in the determination of fully dispersed flow. It will provide insight into the effect of channel height on the velocity profiles as well.

Table 2.

Test matrix of annular flume tests for hydrodynamic measurements in single phase flow

Liquid Phase	Model Oil - LVT 200, Isopar-V, Water
Total Liquid Volume	4.6L
Width of Flow Channel	2.7 in. (0.07 m)
Height of Flow Channel	2.0 in. & 4.5 in. (0.05 m & 0.1 m)
Pitot Tube Height	1/6, 1/3, 1/2, 1.0, 1.5 - 3.75 in.
System Temperature	25°C
System Pressure	1.01 bar

Table 3.

Test matrix for phase wetting experiments in two-phase flow.

Oil Phase	Model Oil - LVT 200, Isopar-V, Crude
Water Phase	Deionized Water with 1% wt. NaCl
Water Cut	2.5% - 20% Increment Size: 2.5 %
Total Liquid Volume	4.6 L
Width of Flow Channel	2.7 in. (0.07 m)
Height of Flow Channel	2.0 in. (0.05m)
System Temperature	25°C
System Pressure	1.01bar

EXPERIMENTAL SETUP AND PROCEDURES

This section discusses the apparatus, measurement techniques, and procedures used for the experimental work.

5.1. Annular Flume Setup

Experiments are conducted in the stainless steel annular flume, shown in Figure 5. The annular flume is comprised of a rotating top plate, a stationary inner wall made of stainless steel, a stationary outer wall made of stainless steel, and a stationary stainless steel bottom plate. The channel is filled with fluid up to the bottom side of the rotating top plate. Flow is induced by rotation of the motor-driven top plate due to shear. The angular velocity of the rotating top plate, and subsequent fluid flow, can be precisely controlled via the motor controller. The conduit has an adjustable height, H , of 2 in. (0.05 m) to 4.5 in. (0.11 m), an inner radius of $R_i = 5.51 \text{ in. (0.14m)}$, and an outer radius of $R_o = 8.27 \text{ in. (0.21m)}$.

The stainless steel bottom plate, representing the bottom of the internal surface of the steel pipe, is equipped with ports for wall conductance probes, as well as separate ports for a wall shear stress probe and a Pitot tube. Phase wetting is determined by a series of the conductivity probes that are flush mounted to the bottom surface of the annular channel. The conductance probes are arranged in 12 horizontal rows of 8 probes, similarly to the flow loop. Determination of the phase wetting regime is possible due to the conductivity of the brine (Deionized water 1% WT NaCl) and the non-conductivity of oil.

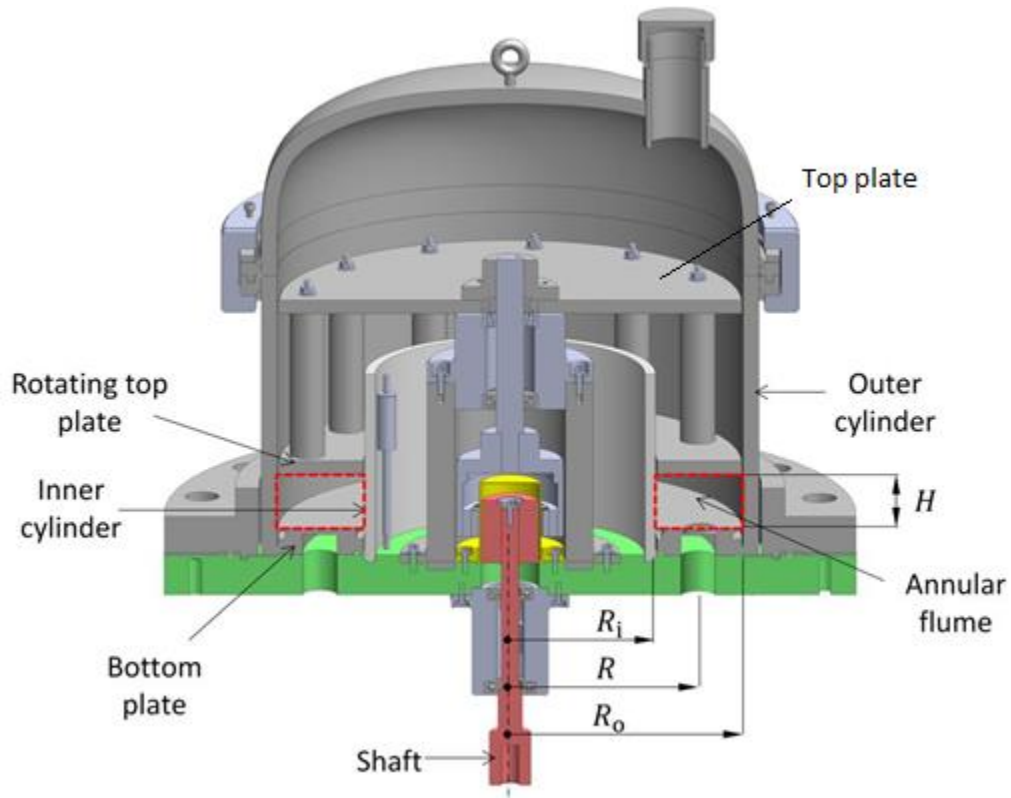


Figure 5. Cross section of annular flume experimental setup (Gardner, 2017).

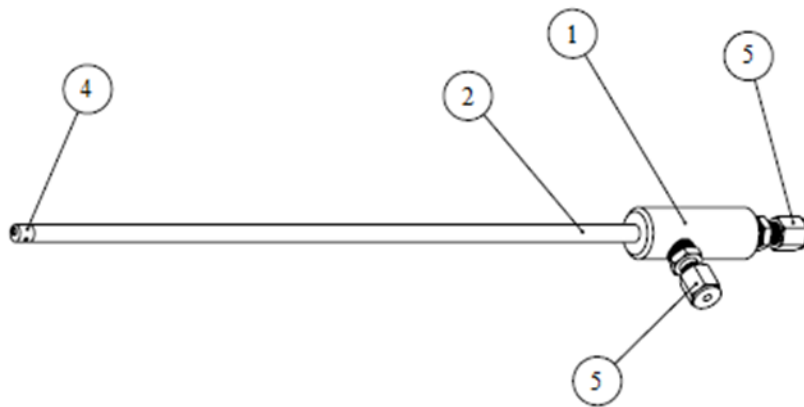
Velocity and wall shear stress measurements are performed in single phase fluid conditions. This portion of the study is performed in single phase flow instead of liquid-liquid two-phase since a homogenous flow model is assumed during fully dispersed two-phase liquid-liquid flow. The homogenous flow model suggests that fully dispersed two-phase liquid-liquid flow behaves like single phase flow (Brauner, 1998). The results of single phase flow experiments can be used to predict the behavior of dispersed two-phase liquid-liquid flow; however, these measurements are mainly taken in an effort to verify the model simulations of single phase flow. Multiphase flow simulations would constitute

the next phase of this study.

The temperature of the flume was not monitored or controlled but was not expected to change considerably during the experiments since the test duration was short. The ambient temperature of the laboratory ranged from 20°C – 25°C.

5.2. In Situ Circumferential Velocity

A Pitot tube is used to measure the in situ circumferential velocity of the fluid during experimentation. The Pitot tube was developed in-house based on standard design, and is shown in Figure 6. The differential pressure transducer being used is a Sensotec transducer with a range of 5 PSID, and an output of 2.0 mV/V. The output of the transducer is being read by a Model GM Sensotec transducer reader. Prior to experimentation, the Pitot tube and accompanying transducer and transducer reader are calibrated to produce a calibration polynomial correlation that links differential pressure to velocity. The Pitot tube is inserted into the flow channel via a port in the bottom of the flow channel



ITEM NO.	PART	DESCRIPTION	QTY.
1	TubeJunction	SS304 ROD 3/4" DIA.	1
2	OuterTube	SS304 TUBE, 0.25 OD, 0.035 WALL	1
3	InnerTube	SS304 TUBE 0.065" OD, 0.005" WALL	1
4	ProbeHead	SS316 0.25 DIA X 0.5Long	1
5	5182K804	1/8" TUBE TO 1/8 NPT ADAPTER	2

Figure 6. Diagram of the Pitot tube used to measure differential pressure.

5.2.1. Pitot Tube Calibration Procedure

A flow channel of 1 in. ID was used to calibrate the pitot tube setup. The flow channel consists of a 50 gallon reservoir of water connected to a 5hp gear pump which recirculates water back to the reservoir via a 1 inch ID pipe fitted with an Omega Mag-PB flow meter and accompanying Model DPF701 Omega RateMeter. The Pitot tube was inserted into the center of the flow field of the 1 inch ID pipe, and connected to the accompanying differential pressure transducer and transducer reader. Data from the flow meter and the Pitot tube transducer reader were collected simultaneously via data acquisition software designed in house. Data were recorded at a sampling rate of 1 Hz for different flow rates at regular intervals for periods of 10 second; the Omega Mag-PB flow meter has a functioning range of 1.6 gpm to 16 gpm. The data acquisition software then

used the output of the transducer reader and the output of the flow meter to produce a linear fit of the data that maps differential pressure to velocity. The resulting calibration curve is shown in Figure 7. The Pitot tube is calibrated within the range of 0.43 m/s to 1.83 m/s, with a standard error of 0.07 m/s.

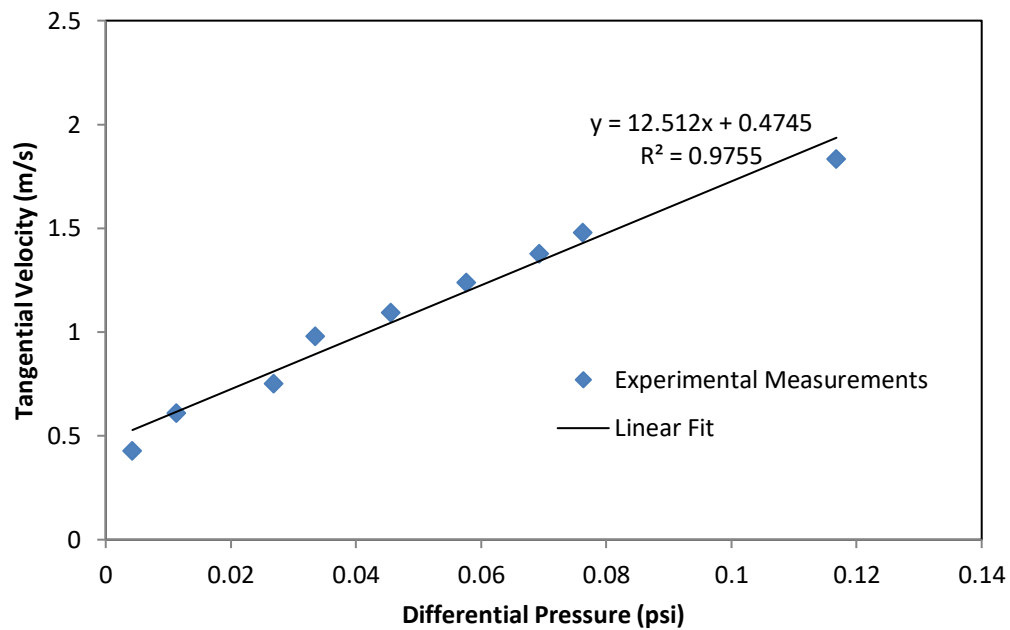


Figure 7. Calibration curve for Pitot tube setup.

5.2.2. Pitot Tube Experimental Procedure

Prior to experimentation, the Pitot tube was inserted into the annular flume through its port in the bottom plate and set at the correct height before sealing the Pitot tube port and the annular flume. The annular flume was then filled with the proper volume of one fluid according to the test matrix; again, the hydrodynamic tests were

performed in single phase flow with either of these fluids: water, Isopar-V or LVT. After filling the annular flume with fluid, care is taken to ensure that there were no air bubbles present within the lines connecting the Pitot tube to the transducer. The opening of the Pitot tube was orientated facing the incoming tangential flow stream. Data from the transducer reader was collected via the data acquisition software. Prior to inducing flow, the transducer reader was zeroed out. Flow was then induced, starting with the lowest achievable top plate rotational speed. Once the top plate rotational speed was set on the motor controller, a period of 2 minutes passed for fully developed flow to occur and the output of the transducer to become stable before beginning data acquisition. The sampling rate was set to 1 Hz. Three data points that were each an average of 30 samples were recorded at each top plate speed. Once a data point was sampled, 1 minute passed before the subsequent data point was sampled. These points are then averaged for each top plate speed. Overall, each experiment lasted approximately 90 minutes.

5.3. Wall Shear Stress

A Lenterra RealShear Sensor-Probe is used to carry out wall shear stress measurements, with a range of 0 to 140 Pa. Shown in Figure 8, this probe uses two micro optical strain gages called Fiber Bragg Gratings (FBG's) attached to a cantilever fit with a floating element. These FBG's are inserted into optical fibers that are attached to the cantilever within the probe. When the FBG experiences strain due to the shear stress applied to the floating element, its optical spectrum changes. This change is measured in wavelength. Because temperature can also change the optical spectrum, two separate FBG's on each side of the cantilever are used to counteract this shift due to temperature.

The true shift in optical spectrum due to shear stress is the difference between the FBG's, given by the following equation (Sheverev, 2012).

$$\Delta\lambda = \lambda_{FBG1} - \lambda_{FBG2} \quad (37)$$

Where λ_{FBG1} is the optical spectrum shift of the first FBG, and λ_{FBG2} is the optical spectrum shift of the second FBG.

The shear stress applied to the cantilever is defined by the following equation.

$$\tau_w = k\Delta\lambda \quad (38)$$

Where k is the calibration coefficient determined by the properties of the FBG's, the area of the floating element, and the elastic modulus, length, and diameter of the cantilever (Sheverev, 2012). This data is acquired by the accompanying Lenterra data controller and Lenterra data acquisition software.

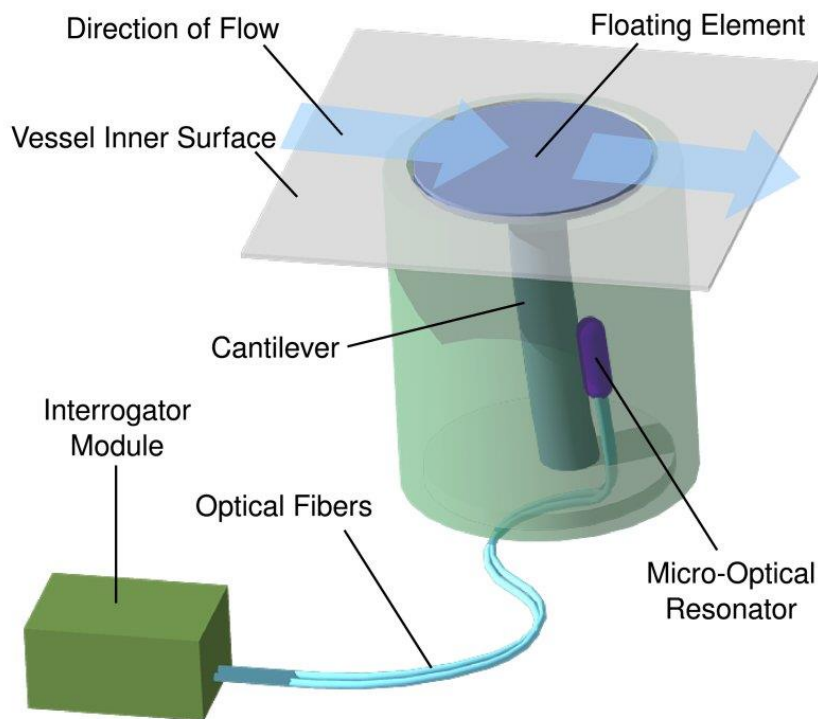


Figure 8. Depiction of Lenterra Wall Shear Stress Probe (Sheverev, 2012).

5.3.1. Wall Shear Stress Probe Preparation Procedure

Prior to mounting in the annular flume, the floating element of the shear stress probe must be centered using the adjustment screws located at the base of the probe. The empty space below the sensor of the probe was then filled with the experimental fluid (either water, Isopar-V or LVT). Next, the shear stress probe was calibrated. The gage coefficient that resulted in the proper maximum shear stress and minimum shear stress must be determined using the accompanying software from Lenterra. To ensure that the proper gage coefficient was used, a “finger test” is performed. A finger test consists of using a cotton swab to move the floating element to its furthestmost position in both the positive and negative directions. The range for this shear stress probe is 0 to 140 Pa, respectively. The finger test must be performed once the probe is installed in its final position, flush mounted in the accompanying port of the annular flume.

5.3.2. Wall Shear Stress Experimental Procedure

After the finger test, the annular flume was sealed and filled with the experimental fluid. Within the wall shear stress probe program, the zero level was refreshed prior to inducing flow. Recording of shear stress measurements was initiated, and then the top plate speed was set to the desired rate. Flow is given 1 minute to fully develop. Wall shear stress data was then extracted from the maximum levels observed during each recording sequence. Each recording sequence observed maximum levels for 1 minute after fully developed flow, before decreasing the top plate speed back to zero velocity. Recording continued until flow has completely ceased. This procedure was repeated 3

times for each top plate speed. Overall, each experiment lasted approximately 95 minutes.

5.4. Phase Wetting Determination Procedure

Conductance probes were used to determine phase wetting maps. Each probe, shown in Figure 9, consists of a stainless steel wire coated in epoxy with a diameter of 0.018 in. The stainless steel wire is fitted with a stainless steel sleeve of 0.0625 in. diameter. 100 k Ω resistors are placed between each probe and the accompanying circuit board. During sampling, the voltage applied to each probe shifted from +12 v to -12 v every 20 microseconds. This allows a closed circuit to develop between the pin and the stainless steel plate bottom plate when the brine, due to its conductivity, wets the probe and the surrounding stainless steel sleeve. On the contrary, when oil wets the probe, due to its non-conductivity, an open circuit occurs between the pin and the stainless steel sleeve. These simultaneous measurements at each probe results in a set of binary measurements; 0 for oil wetting and 1 for water wetting. This information was stored using data acquisition software, and subsequently used to construct the phase wetting map. Oil wetting of the bottom plate and subsequent fully dispersed flow was determined when 90% of the 96 conductance pins are oil wet, as some pins tended to remain water wet even at the highest of top plate rotational speeds.



Figure 9. Wall conductance probe made by inserting a stainless steel wire coated in epoxy into a stainless steel sleeve.

These probes were flush mounted on the bottom plate of the annular flume in 12 rows of 8, as shown in Figure 10.

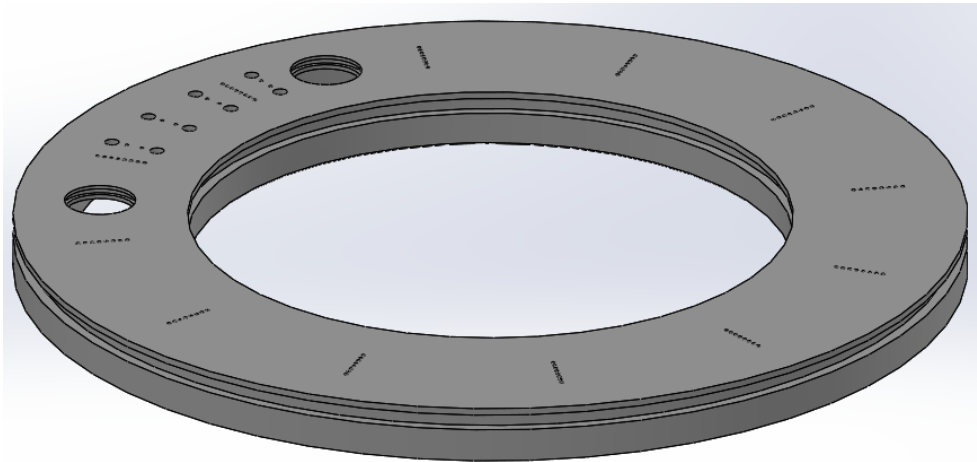


Figure 10. CAD drawing of the stainless bottom plate of the annular flume with large ports for a wall shear stress probe and a Pitot tube, respectively, and 12 rows of 8 ports for conductance probes (Albert Schubert of the ICMT).

5.4.1. Phase Wetting Procedures

The critical entrainment velocity, the velocity at which the water phase becomes fully dispersed in the oil phase and subsequent full oil wetting of the bottom plate occurs, was determined by approaching full dispersion from an initially stratified flow. While the mathematics in the background section describe the opposite scenario (point at which water droplets fall out of suspension, making the flow no longer fully dispersed), the experiment is being performed in this way for a few reasons. Fully dispersed flow in the annular flume is observed when the water phase becomes fully entrained in the oil phase, and subsequent oil wetting of the conductance probes on the bottom plate occurs;

however, the point at which water droplets coalesce, and begin to fall out of suspension cannot be observed immediately, because they do not necessarily wet the conductance probes of the bottom plate immediately. This is due to the settling time of the water droplets. There was a delay between the point at which water droplets fall out of suspension and when they contact the bottom plate. Because of this settling time, the critical entrainment point could be observed with the given experimental setup when going from fully dispersed flow to stratified flow. Fortunately, the critical velocity at which fully dispersion occurs is the same whether moving from stratified flow to fully dispersed flow or vice versa (Brauner, 2001).

5.4.2. Phase Wetting Preparation Procedure

Prior to experimentation, the top surface of the bottom plate, on which the conductance probes are flush-mounted, was lightly wet sanded with 600 grit sand paper and isopropyl alcohol. It was then rinsed and cleaned with DI water and isopropyl alcohol. The reference voltage, the voltage above which the phase wetting data acquisition software will recognize the surface to be wet with water, was then set for the conductance probes. This was done by wetting the surface of the probes using a towel soaked with the solution of DI water + 1% wt. NaCl that will be used during experimentation. The reference voltage potentiometer was adjusted until the phase wetting software recognized water wetting. After the reference voltage was determined, the top surface of the bottom plate was again cleaned with DI water and isopropyl alcohol.

5.4.2.1. Phase Wetting Experimental Procedure

The solution of DI water + 1% wt. NaCl was added to the annular flume first, followed by the model oil, which was poured slowly, to ensure that the layer of water remains in contact with the conductance probes on the bottom surface of the annular flume. An image was taken of the phase wetting map, to capture the initial phase wetting condition prior to testing; often times a few probes became wet with oil while loading the annular flume, in which case, the entire apparatus was flushed, and the cleaning process repeated.

The top plate speed of the annular flume was then increased incrementally until the point of total oil wetting occurs. The phase wetting software was set to record a phase wetting image every five seconds. Each increase in top plate speed was given 10 minutes for phase wetting changes and fully developed flow to occur before increasing to the next motor speed. Changes in phase wetting were often observed almost immediately after the motor speed was set and may have continued to occur even beyond five minutes, but very rarely were changes recorded beyond 10 minutes, hence the reasoning for the specific time. Phase wetting images were taken during the entire duration of phase wetting changes to accurately observe period between equilibrium when phase wetting changes were occurring on the bottom plate. Oil wetting of the bottom plate and subsequent fully dispersed flow was determined when 90% of the 96 conductance pins were oil wet. This was due to some pins remaining water wet even at the highest of top plate speeds. These pins were then disregarded. Overall, each experiment lasted approximately 150 minutes.

5.4.3. *Safety (disposal)*

All liquid within the annular flume was drained and disposed of in the proper container. The interior of the annular flume was then cleaned with DI water and isopropyl alcohol.

EXPERIMENTAL RESULTS AND DISCUSSION

6.1. Hydrodynamic Study: Velocity Profiles

The tangential velocity profiles from experiments with the brine (DI water + 1wt.% NaCl) are shown in Figure 11. The irregularity in the velocity profile at conduit heights equal to 0.50 inch and below was due, in part, to the transverse flow. The transverse flow is discussed in further detail in section 6.4.2.

The results of the velocity measurements in the 4.5 in. conduit, shown in Figure 12, exhibited larger velocity gradients from the top to the bottom of the conduit than the results shown in Figure 11 for the 2 inch conduit. This may have occurred because of the increased conduit height, and the increased power input into the fluid from the rotating top plate, as the increased fluid mass in the 4.5 in. conduit requires more power to induce flow.

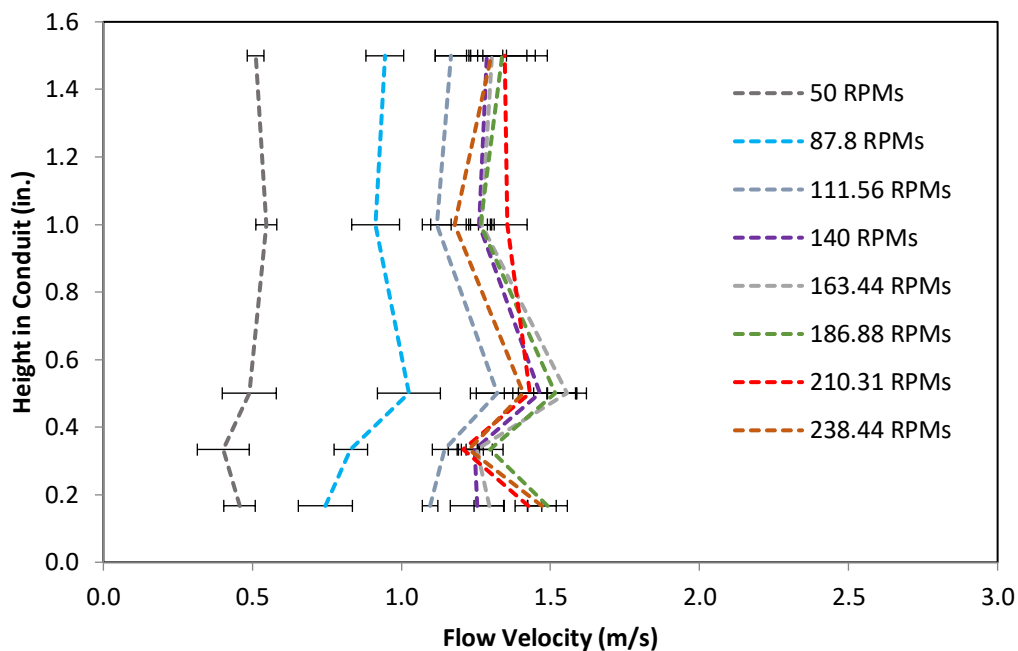


Figure 11. Plot of experimental results of tangential velocity profiles of brine at varying heights and top plate speeds in the 2.0 in. conduit.

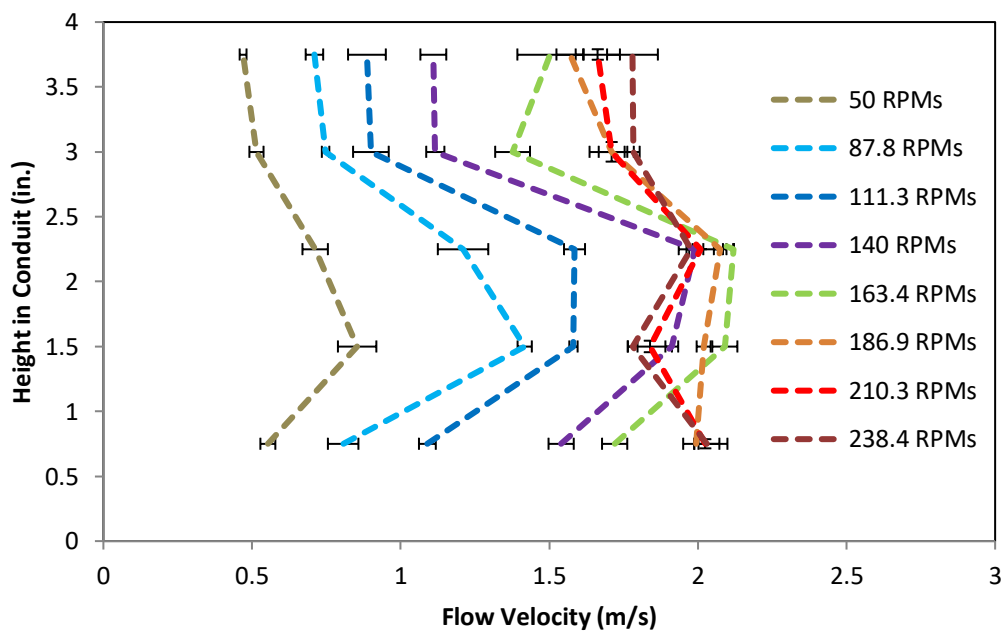


Figure 12. Plot of experimental results of tangential velocity profiles for the brine at varying heights and top plate speeds in the 4.5 inch conduit.

Experimental data collected with LVT-200 in the 2in. and the 4.5in. conduit are shown in Figure 13 and Figure 14, respectively. The LVT-200 results exhibited more uniform profiles with less variation in flow velocity from the top of the conduit to the bottom of the conduit in comparison to the experiments performed with brine. This may have been due in large part to the difference in viscosity between the brine and LVT-200.

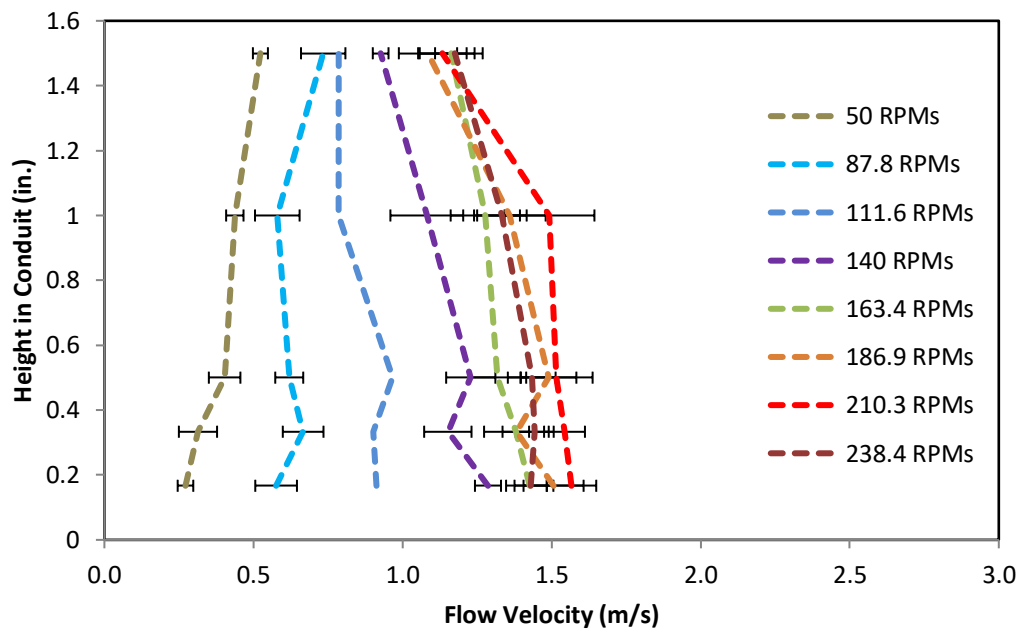


Figure 13. Plot of experimental results of tangential velocity profiles for the LVT 200 at varying heights and top plate speeds in the 2.0 in. conduit.

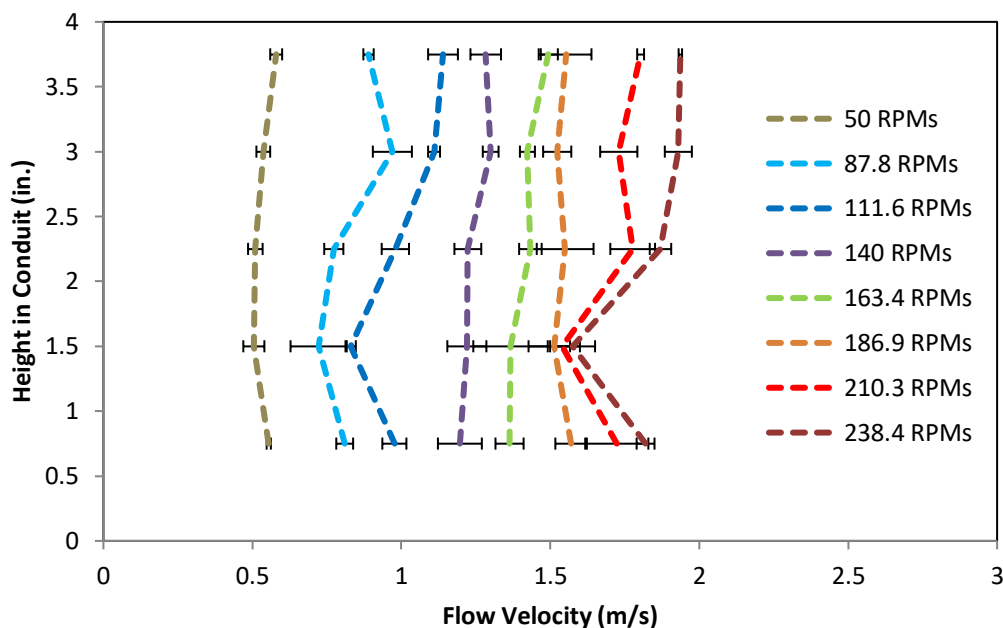


Figure 14. Plot of experimental results of tangential velocity profiles for the LVT 200 at varying heights and top plate speeds in the 4.5 inch conduit.

The velocity measurements acquired with Isopar-V are shown in Figure 15 and Figure 16. Viscosity may have been a large factor in this result, as the viscosity of Isopar-V, 13.3 cP, is over four times that of LVT-200 at 2.7 cP, and over 10 times that of brine at 0.89 cP. Isopar-V exhibited slightly more stable velocity profiles with lower variability at each data point than those of LVT 200 or brine. The profiles of Isopar-V also exhibited less of a velocity gradient from the top of the conduit to the bottom of the conduit than the either LVT-200 or the DI water brine.

The high viscosity of Isopar-V resulted in velocity profiles with less variation in velocity from the top of the conduit to the bottom. The velocity gradient between top and bottom plates is inversely proportional to viscosity.

Larger gradients were exhibited in the velocity profiles of the results in the 4.5 in. conduit in comparison with the results in the 2.0 inch conduit.

The measured tangential velocity should increase as the rotational speed of the top plate increases. A higher flow velocity was expected near the top plate, as a lower flow velocity is expected near the bottom plate due to wall effects. The velocity profile between the top and the bottom of the conduit should have been relatively flat. The results deviate from these expectations in a few ways. The bump exhibited in each of the velocity profiles near the bottom wall, and, to a lesser extent, near the rotating top plate, could have occurred due to the transverse flow present in the conduit. This is more apparent at lower top plate rotational speeds. Deviations from the expected result of the velocity profiles could also have occurred due to orientation of the Pitot tube in relation to the flow. If the Pitot tube was not orientated downstream of the flow with the opening in the top completely orthogonal to the flow, it would not have properly measured tangential velocity.

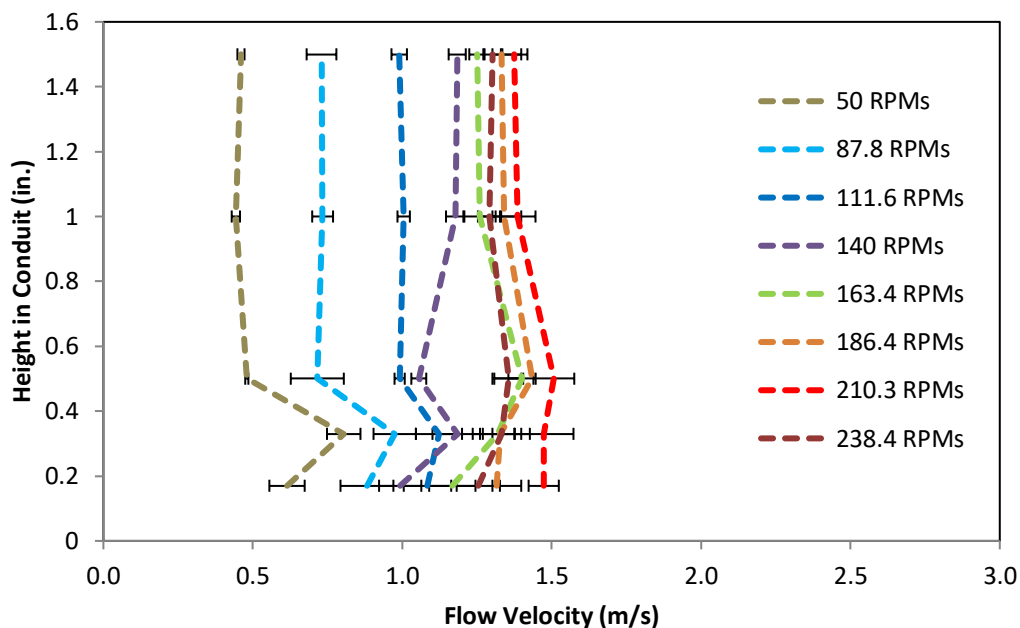


Figure 15. Plot of experimental results of tangential velocity profiles for the Isopar-V at various rotating top plate speeds in the 2.0 in. conduit.

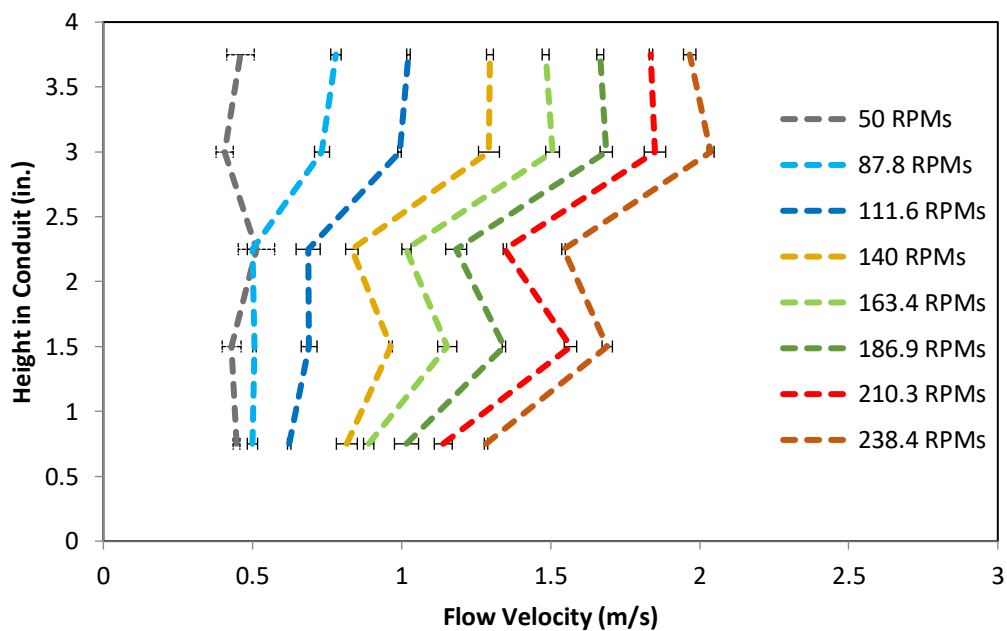


Figure 16. Plot of experimental results of tangential velocity profiles for the Isopar-V at varying heights and top plate speeds in the 4.5 in. conduit.

There was a transverse flow which has its greatest values at the top of the conduit and affects these velocity profiles. This transverse flow developed as fluid was pushed from the top plate towards the outer wall, down the outer wall towards the bottom plate, across the bottom plate towards the inner wall, and up the inner wall towards the top plate. The transverse flow would have been highest near the top plate and outer wall, and lowest near the bottom plate. Because of this flow, a fraction of the tangential velocity may have been converted into transverse flow. This type of velocity profile is exhibited and discussed in the CFD results of tangential velocity of section [6.4.1](#).

6.2. CFD Model Parameters

An important part of the CFD simulations is the design of the mesh applied to the annular flume geometry, shown in Figure 17. It was created using the CFD program, Ansys Fluent, and consisted of 277,000 cells and exhibited densification of cells near the top and bottom walls of the conduit. This was done due to the large velocity gradients found near the walls that occurred due wall effects that is due to the no-slip condition being applied in these simulations. The viscous sublayer was taken into account when designing these meshes. Due to the top plate being the source of shear and subsequently inducing flow, there was higher densification of cells near the top plate as compared to the density of the cells near the bottom plate in effort to provide more accurate results. A sizably smaller velocity gradient is expected to occur through the middle of the conduit, hence the use of less dense cells in this area.

The number of cells chosen, 277,000, was a number that was high enough to provide good approximations of the hydrodynamics of the annular flume while being low

enough for the simulations to be carried out in a timely manner and without failure of the computer program. Simulations on meshes with higher cell counts resulted in failure of the Ansys Fluent program.

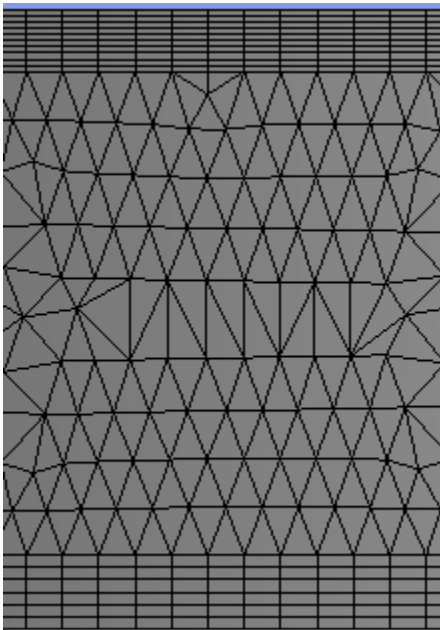


Figure 17. A profile of the rectangular cross-section of the mesh used in the current study.

The minimum layer thickness is 0.5 mm at the top of the conduit and 1 mm at the bottom of the conduit.

Figure 18 shows the top views of the mesh. Cell densification of the mesh near the inner and outer walls was not employed. This study was mainly concerned with characteristics of the flow in the middle of the conduit where effects of the inner wall and outer wall are minimized. This type of flow resembles that of Couette flow, which is fluid

flow between two plates in which one plate moves parallel to the other, thus inducing flow.

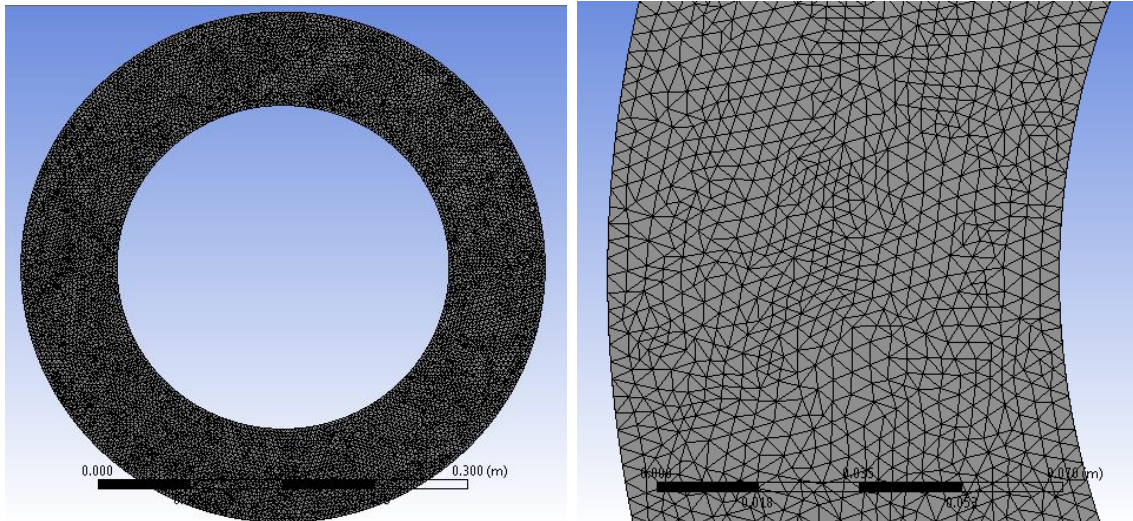


Figure 18. Left: Top view of the CFD mesh used in the current study. Right: Magnified view of top mesh of current study.

6.3. Validation of CFD Model: Velocity Results

The following section serves to validate the results of the numerical modeling by comparing experimental and modeling results of tangential velocity. The CFD results of tangential velocity and transverse velocity are discussed. The no-slip condition applied in the CFD simulations stipulates that:

- The fluid velocity is zero at the inner wall, outer wall, and bottom plate;
- The fluid velocity at the top plate is determined by the rotational speed of the top plate.

Validation of the turbulence model used in the CFD simulations was accomplished, in part, by comparing the experimentally measured values of tangential velocity with the

predicted values from the model. Experimental results and model results were compared at three different top plate speeds spanning the range of top plate speeds experimentally measured with the Pitot tube. These included 87.8 rpm, 163.4 rpm, and 210.3 rpm. Based on the results of other studies done on apparatuses with similar geometry, the standard $k - \epsilon$ model is used to find solutions for these annular flume speeds (Yang et al., 2000). These previous studies, such as de Dood (de Dood, 1997), found good agreement between experimental results and model results at similar angular velocities, as well. The model results and the experimental results of the current experiment were acquired in single-phase flow consisting of the brine, LVT-200, and Isopar-V.

Figures 19- 21 show the experimental measurements plotted alongside the modeling results of tangential velocity for selected conditions in single phase flow (brine, LVT-200, and Isopar-V, respectively). Model results for tangential velocity are depicted as a solid smooth line, and experimental results are plotted as points along dashed lines. The colors correspond to top plate speed. The bumps in the model results at 0.1 in. and 1.9 in. are indicative of the effect of the transverse flow on the tangential flow. The transverse flow is highest at the top of the conduit, where it resulted in a slight decrease in tangential flow. At the bottom of the conduit, transverse flow may have augmented the tangential flow. The $k - \epsilon$ turbulence model provided good agreement with experimental results. The uncertainty of the Pitot tube was found to be ± 0.066 m/s, based on the calibration results, which rules out the error in the Pitot tube as a significant source of discrepancy between experimental results and predicted results.

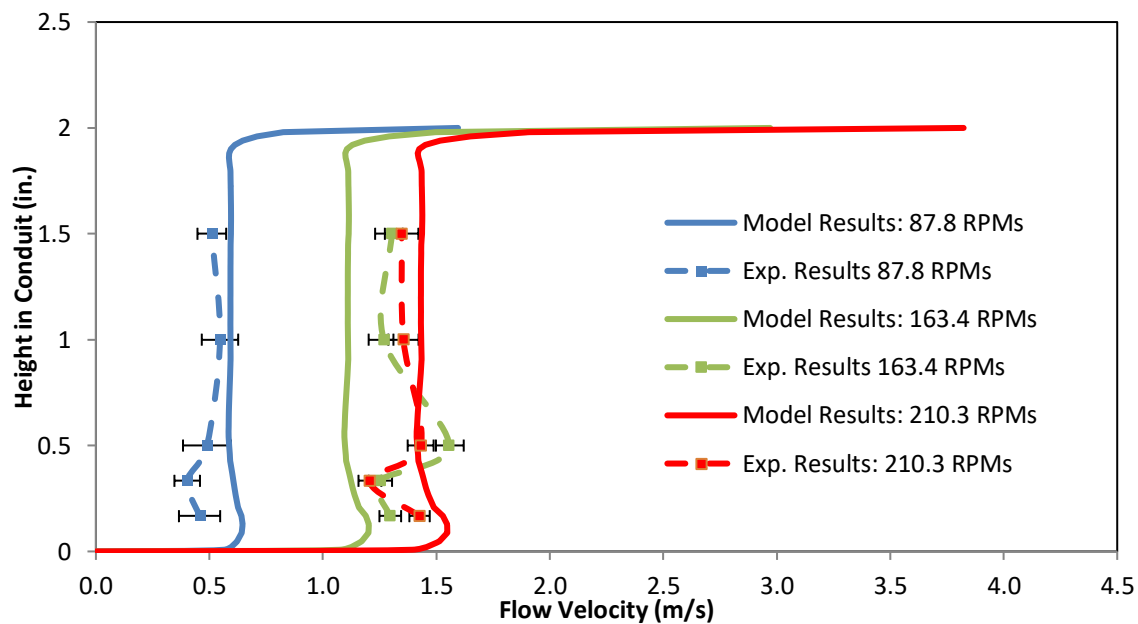


Figure 19. Plot of model results and experimental results single phase tangential flow velocities of DI water + 1% NaCl at varying heights for top plate rotational speeds of 87.8 RPMs, 163.4 RPMs, and 210.3 RPMs. Model results are plotted as smooth, solid lines. Experimental results are plotted as points along a dashed line.

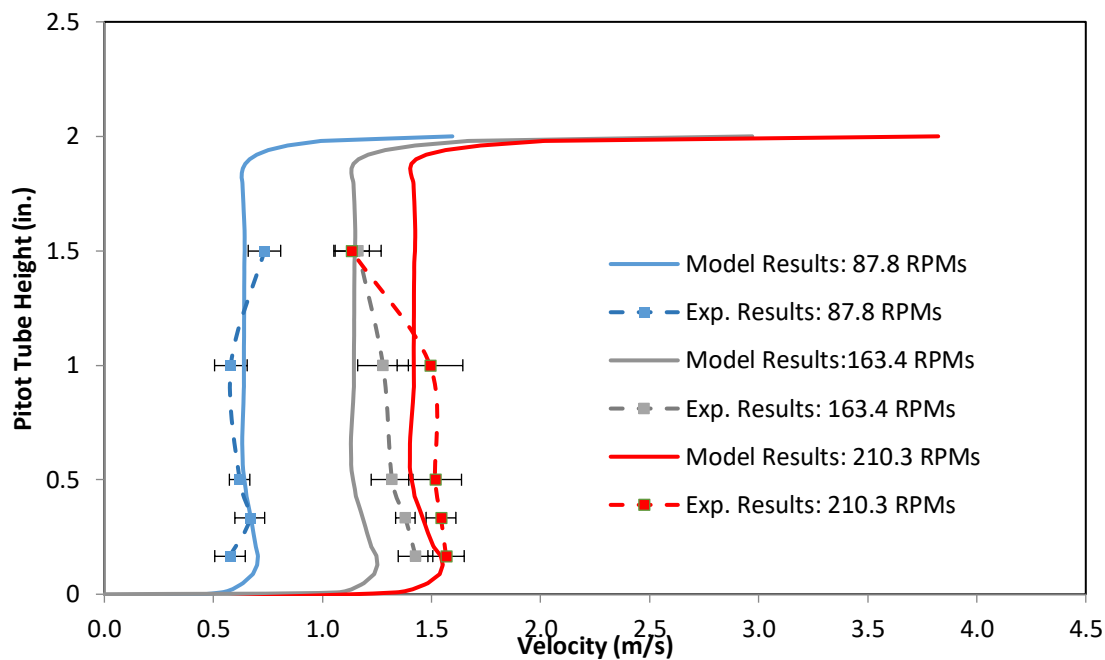


Figure 20. Plot of model results and experimental results single phase tangential flow velocities of LVT-200 at varying heights for top plate rotational speeds of 87.8 RPMs, 163.4 RPMs, and 210.3 RPMs.

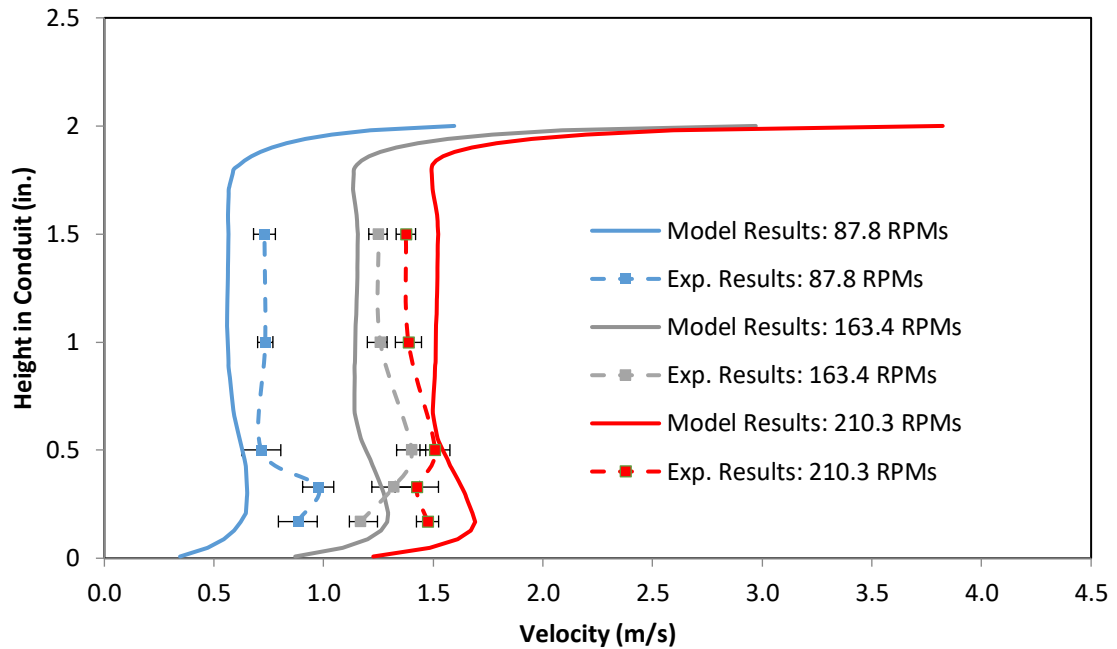


Figure 21. Plot of mode results and experimental results of single phase tangential flow velocities Isopar-V at varying heights for top plate rotational speeds of 87.8 RPMs, 163.4 RPMs, and 210.3 RPMs.

6.4. Modeling of Tangential and Transverse Flow in the Annular Flume

This section serves to characterize modeling results of the tangential velocity component of the flow in the annular flume, and the secondary transverse velocity component that results from the shear driven flow in the annular conduit.

6.4.1. Modeling of Tangential Flow

Modeling results of tangential velocity are presented below. These results are used in the determination of Blasius type correlations for Fanning friction factors in the subsequent section. The fluid velocity near the top plate is expected to increase radially across the conduit. Figure 22 shows a tangential velocity contour in the annular flume. This contour was created for Isopar-V at a rotational speed of 87.8 rpm.

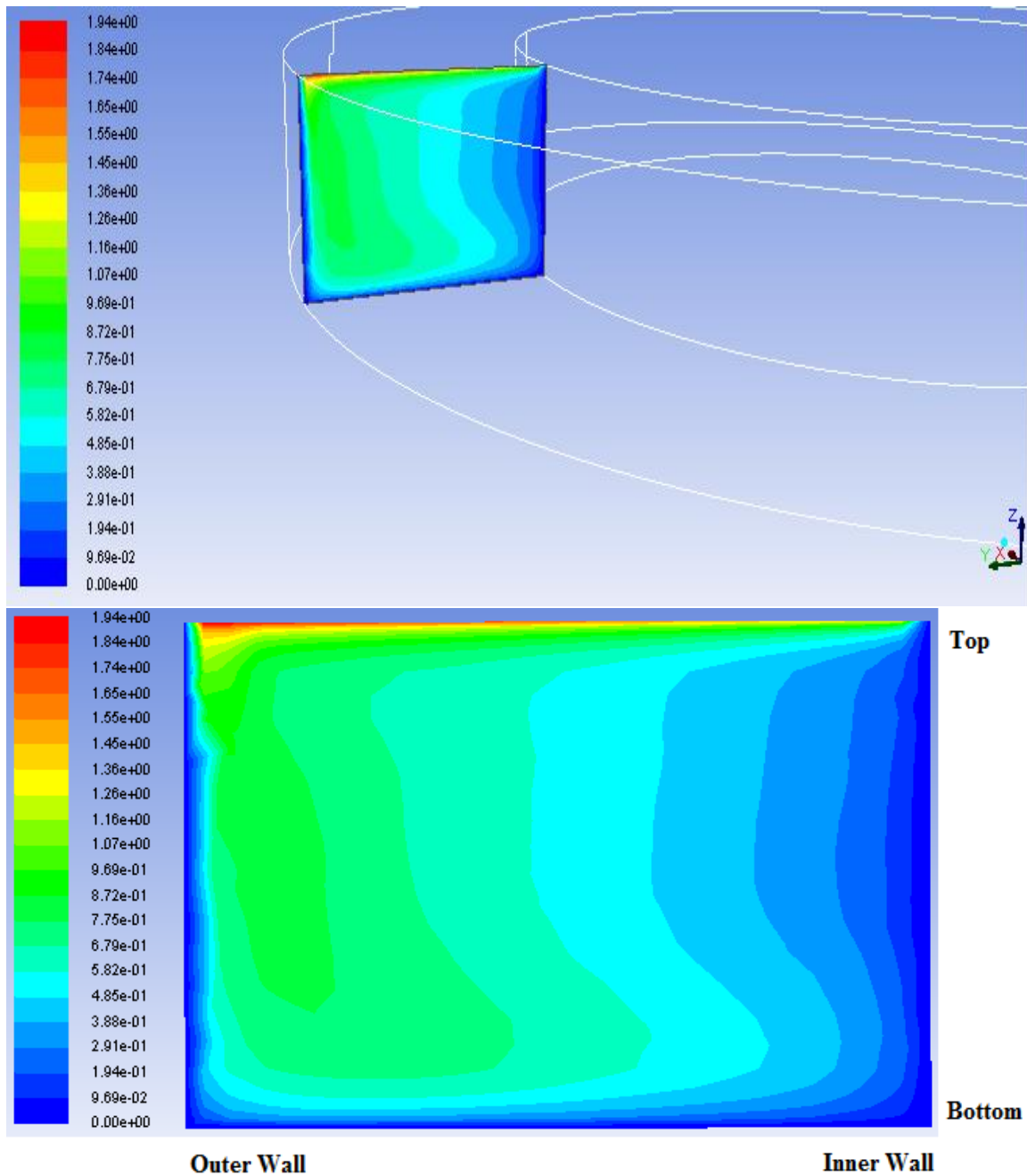


Figure 22. Model results: Contour of tangential velocity of Isopar-V flow across the conduit at a top plate rotational speed of 87.8 rpm.

The maximum tangential velocity encountered in this case, which occurred near the top plate and at the outer wall, was approximately $1.94 \frac{m}{s}$; whereas the tangential

velocity of the flow 1 cm away from the bottom of the conduit in the same radial position was $0.35 \frac{m}{s}$. Due to the non slip condition, the tangential velocity of the top plate at the same radial position was the same as the tangential flow velocity at the top of the conduit. The tangential velocity near the bottom of the conduit was approximately 14% of the top plate tangential velocity, at the mid radius. In general, the annular flume exhibited a pattern of increasing tangential velocity with increasing radius across the conduit. This sort of gradient in velocity was expected, given the circular geometry of the annular flume; it is a basic principle of physics that the tangential velocity of a rotating wheel increases with radius.

6.4.2. *Modeling of Transverse Velocity*

This section discusses the cross flow that resulted due to the annular flume circular geometry. It is discussed in terms of transverse velocity. Figure 23 shows the CFD results of transverse velocity of the conditions described in Figure 22 (Isopar-V at a top plate rotational speed of 87.8 rpm). The most apparent observation of this plot is the cyclic nature of the transverse flow, as it flowed from the top plate towards the outer wall, down the outer wall towards the bottom plate, across the bottom plate towards the inner wall, and up the inner wall towards the top plate. This was the characteristic pattern of transverse flow observed in the annular flume.

Much like the results for tangential velocity, the highest levels of transverse velocity were observed near the outer wall at the top plate. However, the behavior of the transverse flow slightly above the bottom plate is of more concern to this study, as this is

the area where water entrainment occurs. Characterizing the flow, especially the cross flow, near the bottom plate is important because it is indicative of the velocity of the particle relative to the continuous phase and could be an important component of the vertical component of the transverse flow that could be used in model phase wetting predictions. The steps taken to estimate these values are outlined in the Appendix 2.

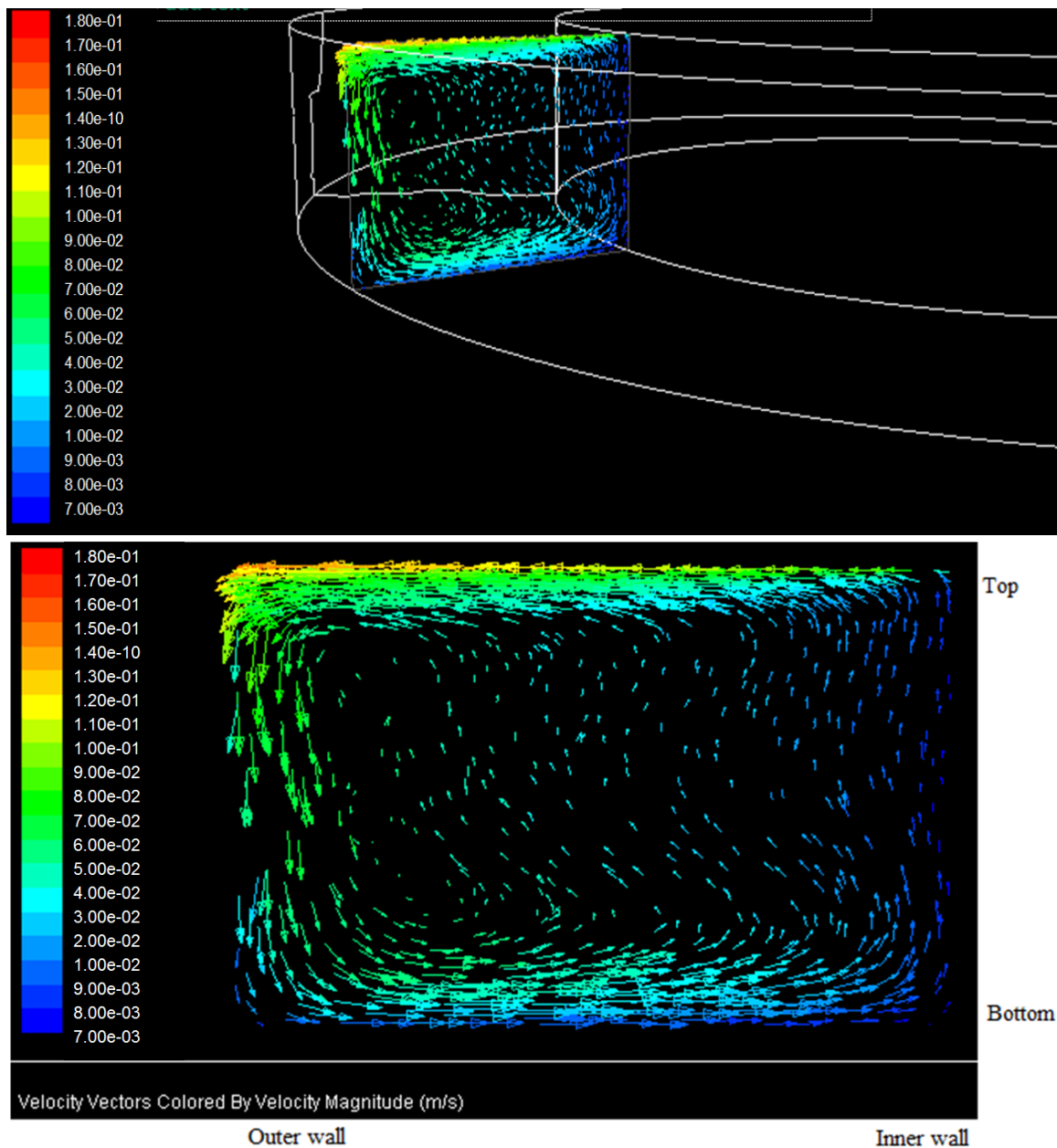


Figure 23. Model results of transverse velocity (m/s) vector field for Isopar-V at a top plate rotational speed of 87.8 rpm.

6.5. Hydrodynamic Study: Wall Shear Stress Profiles

The results of the wall shear stress experiments in the annular flume with the conduit height set to 2.0 inches are shown in Figure 24. These experiments were

conducted using the flush mounted Lenterra wall shear stress probe. The profile of each line showed an expected trend of wall shear stresses wherein wall shear stress increased with top plate speed (and subsequent flow velocity). These results show brine flow generating higher levels of shear stress than either LVT-200 or Isopar-V, which is unlikely, given their respective viscosities and velocity profiles; however, no firm conclusion can be taken from the wall shear stress results due to the large levels of variability exhibited in these data. This model of Lenterra shear stress probe is specified for ranges of 0 to 140 Pa, with a resolution of 5 Pa, while the levels exhibited in the annular flume in the present study are very small. This could result in large variability in the measurements. Potential issues with the measurement technique are discussed in section 6.8.

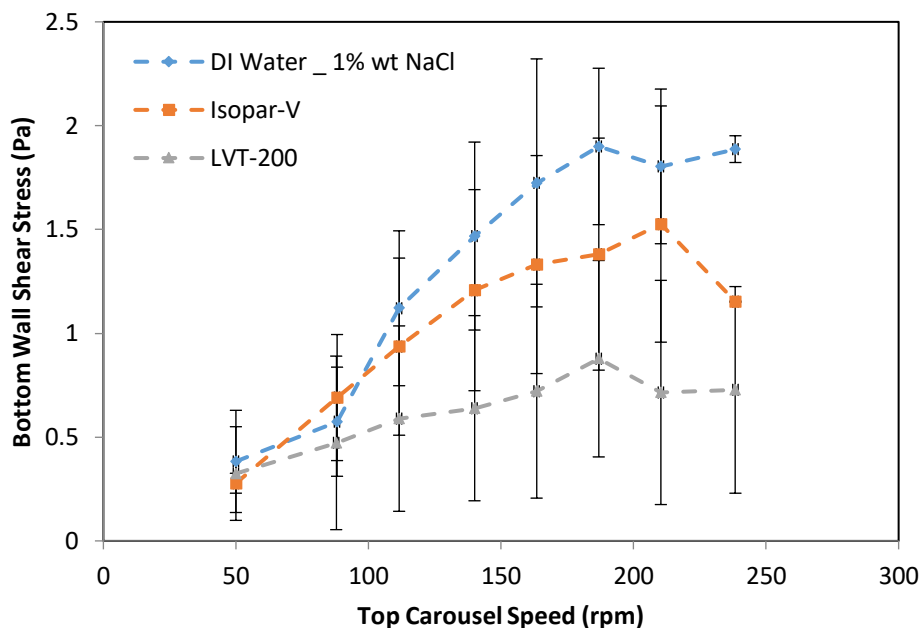


Figure 24. Experimental results of average bottom wall shear stress plotted as a function of top plate rotational speed with the conduit height of the annular flume set to 2.00 in.

Figure 25 shows the results of the wall shear stress experiments in the annular flume with the conduit height set to 4.5 inches. These experiments were conducted using the flush mounted Lenterra wall shear stress probe in the same manner as in the 2.0 in. conduit. Due to the difference in conduit height, the results of the wall shear stress experiments in the 4.5 in. conduit should have produced wall shear stress values larger than those shown in Figure 24 based on the augmented power input in the 4.5 in. trials due to the increased volume (and mass) of the fluid in the channel. This trend was observed in the shear stress profile of Isopar-V and LVT-200, but not brine; however, there was also a large amount of variability at each data point, which is an average of six measurements. These results do, however, represent reality in some respects. Based on viscosity alone, Isopar-V would be the fluid phase expected to result in the highest

average bottom wall shear stress at each top plate speed followed by LVT-200, and the brine.

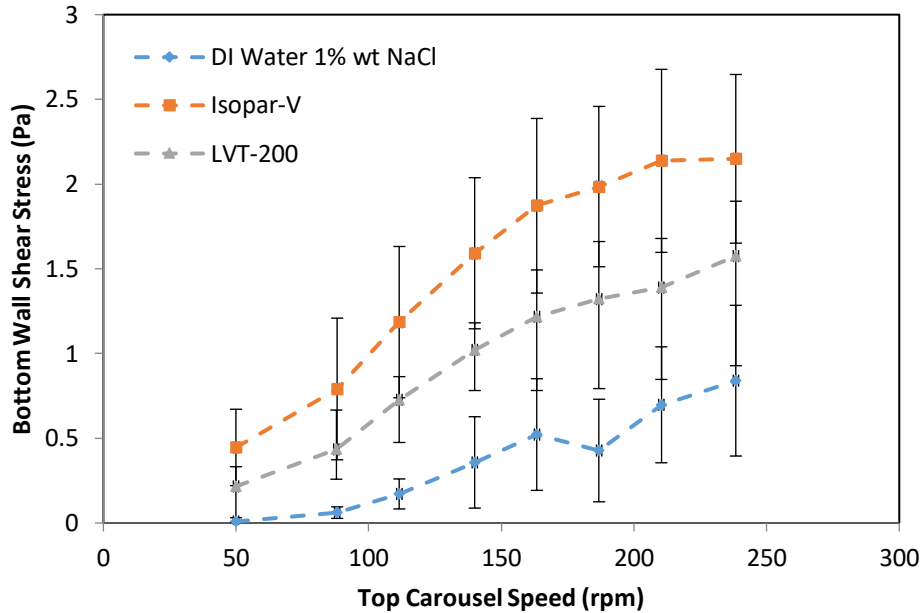


Figure 25. Experimental results of average bottom wall shear stress plotted as a function of top plate rotational speed with the conduit height of the annular flume set to 4.5 in.

6.6. Validation of CFD Model: Bottom Wall Shear Stress

Measurements of wall shear stress were acquired using the Lenterra shear stress probe at regular intervals across the same range of top plate speeds as the velocity study. These values were compared against $k - \varepsilon$ turbulence model results for top plate speeds of 87.8 RPM, 163.4 RPM, and 210.3 RPM, respectively, in Figure 26. Model results are depicted as a solid line, and experimental results are plotted as points along dashed lines. The colors correspond to different fluids. In some instances, the model results and experimental results differed by an entire order of magnitude. The $k - \varepsilon$ turbulence

model has performed well in simulations of similar studies (Kuei-Yuan, 1982). Based on the good agreement obtained in the tangential velocity study, it is believed that the large discrepancies between experimental results and model results are due to the experimental method: the Lenterra shear stress probe. The Lenterra shear stress probe has a measurement range of 0 to 140 Pa with a resolution of 5 Pa. Because these measurements were performed on fluid flow with predicted maximum shear stresses of ~8 Pa, the uncertainty in the probe could have resulted in large discrepancies between experimental results and model results. Nevertheless, the $k - \varepsilon$ turbulence model was used to model the annular flume hydrodynamics based upon the good agreement with experimental results for velocity.

Viscosity is an important factor in wall shear stress, as evidenced by Figure 26. The viscosity of Isopar-V was an order of magnitude higher than either the brine (DI water + 1wt.% NaCl) or LVT-200, which resulted in elevated levels of wall shear stress in Isopar-V. While the viscosities of DI water and LVT-200 are both small relative to Isopar-V, the viscosity of LVT-200 is slightly larger than that of DI water (2.7 cP and 0.89 cP, respectively). These results show only slightly elevated levels of shear stress in LVT-200 relative to DI water.

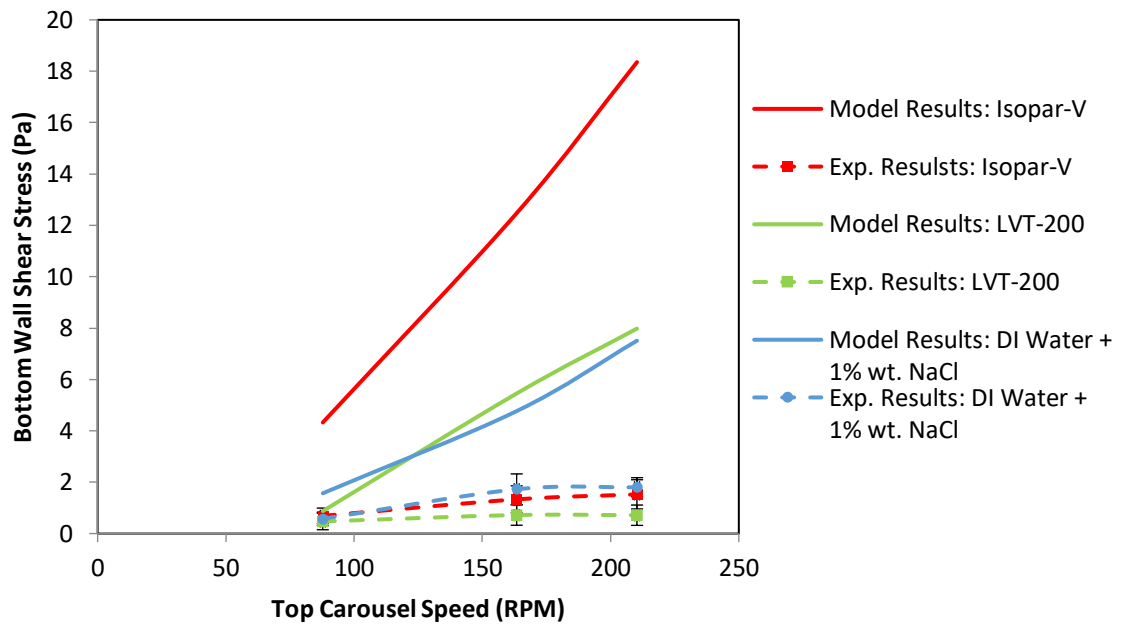


Figure 26. Model Results plotted alongside experimental results for wall shear stress measurements in the 2.0" conduit. Note that the experimental data differs by an order of magnitude from the experimental data.

6.7. Modeling of Bottom Wall Shear Stress

Figure 27 shows CFD results of bottom wall shear stress across the width of the conduit for Isopar-V at varying top plate rotational speeds. The point 0.0 cm corresponds to the inner wall and the point ~8.0 cm corresponds to the outer wall of the annular flume. Much like velocity, the bottom wall shear stress increased moving radially towards the outer wall, reaching a maximum before wall effects cause the bottom wall shear stress to diminish.

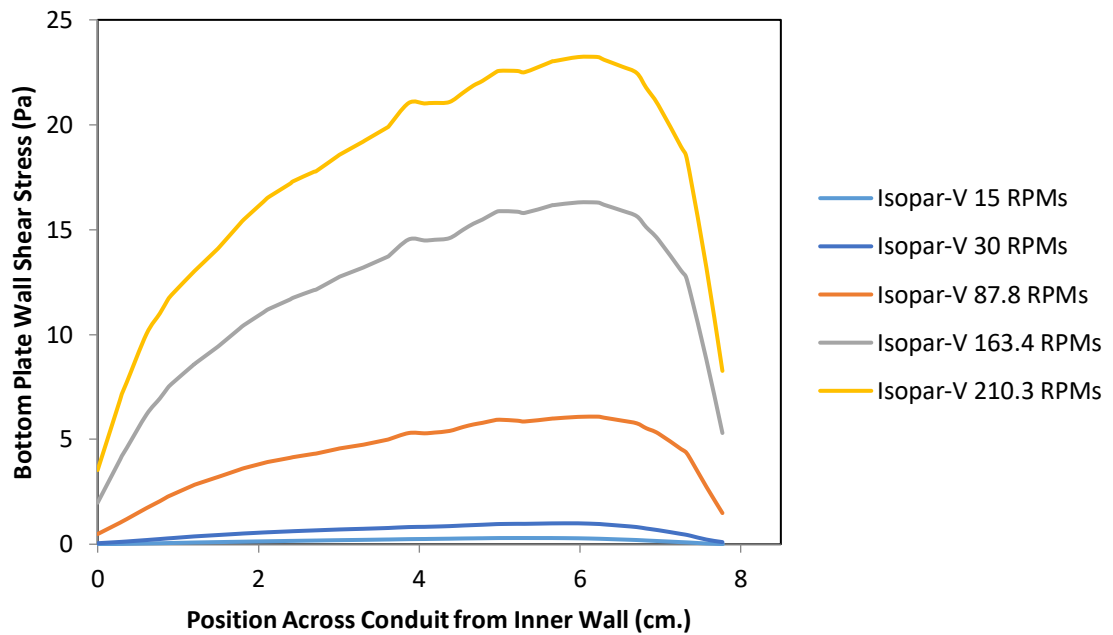


Figure 27. Plot of bottom wall shear stress as a function of position across the conduit for Isopar-V produced by CFD simulations.

6.8. Discrepancies between Model Results and Experimental Results for Shear Stress

This specific Lenterra probe is generally used for values of shear stress of larger orders of magnitude than those values exhibited in the annular flume. This could have resulted in high error values and inaccurate results. It is recommended that a more specific probe be used in future shear stress experiments on the annular flume.

One possible source of error lies in the mechanism by which the wall shear stress probe functions. As stated before, the probe measures wall shear stress by relating it to the displacement of the floating element, which is displaced by fluid flow. More specifically, it measures the total displacement of the floating element in one direction. The shear stress probe is generally used in fluid applications involving fluid flowing in a straight channel, as opposed to the annular channel of the annular flume. Because of the

presence of the secondary cross flow in the annular flume, the velocity vector did not point in the direction tangential to the inner diameter. As a result, the wall shear stress probe would have been best oriented with this resulting skewed flow, rather than tangential to the flow. Unfortunately, due to the turbulent and unusual cross flow nature of the flow, it may have been difficult to position the probe in such a way that would allow accurate measurements to be taken.

The question of the probe's calibration has been raised during the period of experimentation. The probe was purchased having already been calibrated, and numerous shear stress experiments were conducted with the calibrated probe. Upon observing the poor quality of the results, guidance from the manufacturer was requested and a technician was sent from Lenterra to calibrate the shear stress probe, and to show ICMT researchers how to calibrate the probe. Despite the efforts of the technician, the subsequent shear stress measurements at low shear stress levels were as inaccurate as they were prior to his visit. At this point, it was possible that this probe may not be suitable for the flow of the annular flume. This could be due to the type of flow in the annular flume, or the resolution of the probe being too large for the magnitude of shear stress found in the annular flume.

To determine whether the particular probe being used was malfunctioning or if this type of probe does not accurately measure the magnitude of shear stress in the annular flume, in general, two wall shear stress experiments were performed on Isopar-V with a different probe of the same specifications as the probe used in all other wall shear stress experiments. Isopar-V was chosen because it was expected to generate a

sufficiently high wall shear stress values. These experiments were conducted in the 2.0 in. conduit in the exact same manner as the previous experiments. The results, shown in Figure 28, suggest that the different probe was not better at measuring wall shear stress in the annular flume than the previous probe. It is apparent that the Lenterra wall shear stress probe used in the current study is not suitable for use in the annular flume based on these observations.

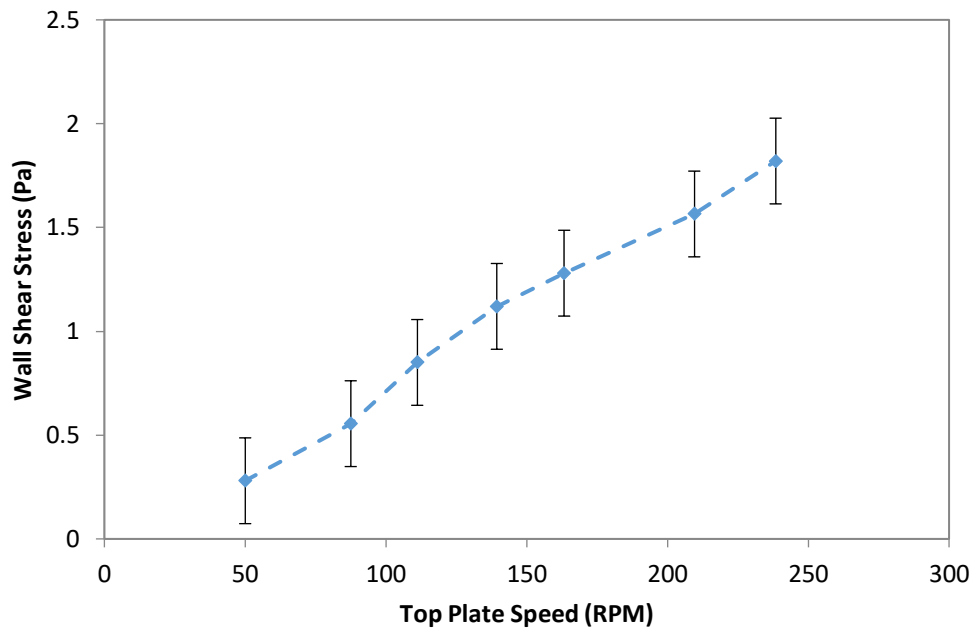


Figure 28. Plot of wall shear stress (Pa) as a function of top plate rotational speed (RPM). Data was acquired using a different wall shear stress probe of the same specifications as the probe used in all other wall shear stress experiments.

6.9. The Effect of the Gap between the Top Plate and the Outer Wall on Flow Velocity and Shear Stress

The gap between the rotating top plate and the outer stainless steel wall of the annular flume is shown in Figure 29. It is postulated that, due to the increased centrifugation at high top plate speeds, fluid will be pushed into this small gap. If enough fluid is pushed into the gap, contact between the bottom surface of the top plate and the fluid surface could be intermittently lost, resulting in subsequent loss in efficiency. When this occurs, an increase in top plate speed would not result in subsequent increased flow velocity. This may be the reason behind the overlapping velocity profiles at top plate speeds above 140 RPM in plots of tangential velocity in Figures 11-13, respectively.

Ideally, one would have expected the velocity profiles to be staggered from one another, as with increasing top plate speed there would be a subsequent increase in flow velocity. This artifact occurring at the bottom surface of the top plate would then be affecting shear stress measurements at the bottom plate.

As Isopar-V is more viscous than LVT-200, one would expect the propensity of LVT-200 to fill the gap to be higher than that of Isopar-V. If this were the case, the effect of the gap would produce less of a loss of fluid flow, and subsequent loss of bottom shear stress, in the presence of Isopar-V, and affect LVT-200 more.

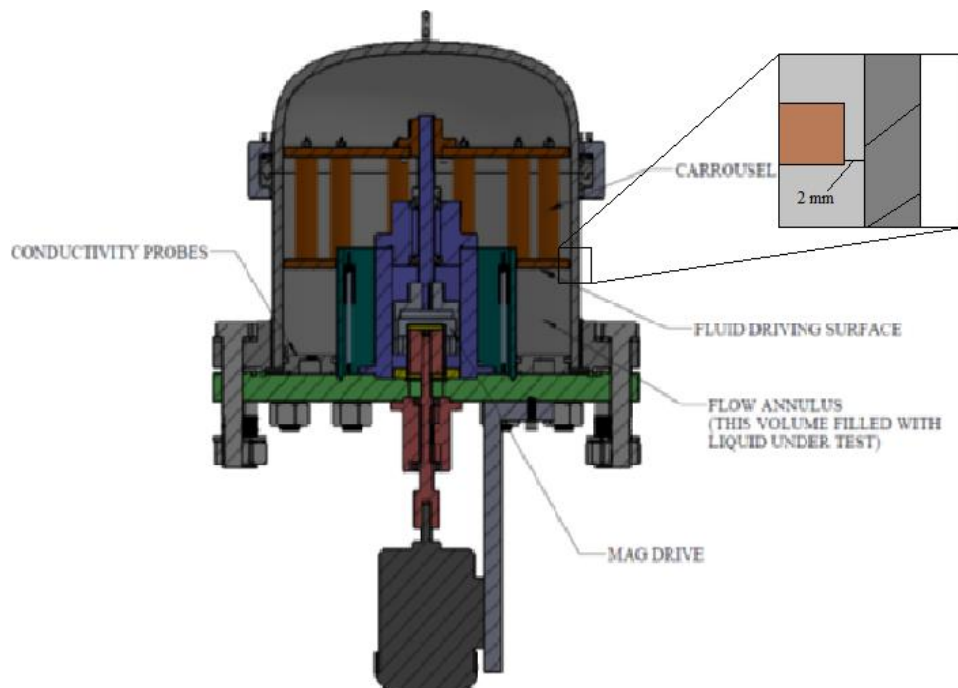


Figure 29. Cross section of the annular flume showing gap between top plate and outer wall (Al Schubert of the ICMT).

De Dood (1997) was able to run simulations of his annular flume with and without the presence of the gap. His slits had a width of 2 mm width and a height of 25

mm, and his conduit had a height of 30 mm. Dood conceded that the effect of the gap on diminished flow velocity would be more apparent in local shear stresses at the bottom plate (Dood, 1997). This implies that the loss in flow velocity due to the effect of the gap could affect phase wetting. It is important to consider that the height of the gap in Dood's study was 25 mm while the gap of the current study has a height of ~12 mm. With a lower height, the fluid phase has a shorter distance to travel to reach the top surface of the rotating top plate. This would allow more fluid to be displaced from the flow channel of the annular flume than the flume in Dood's study (1997), resulting in an increased effect of the gap on the flow.

This gradient in velocity is transmitted along the conduit to the bottom of the cell, resulting in a bottom wall shear stress gradient that increases radially across the conduit, which can be seen in Figure 27.

6.10. Phase Wetting Maps

The following section presents the experimental phase wetting results for two-phase oil/water flow. Figure 30 through Figure 32 show the maps of phase wetting based upon water cut and mean mixture velocity for a proprietary crude oil, LVT-200, and Isopar-V, respectively. Areas of water wetting are denoted with circles and areas of oil wetting are denoted with squares. The solid line represents the transition from oil wetting to water wetting. Comparing the three graphs, it is notable that the velocity at which water entrainment occurs is inversely proportional to oil/water interfacial tension. This behavior was observed in crude oil, which has the highest interfacial of the oils used in phase wetting experimentation, and in LVT 200, which has the lowest interfacial of the

oils used in phase wetting experimentation. Also notable is the trend in increasing flow velocity required for entrainment with increasing water cut in the figures of crude oil and LVT-200; however, Isopar-V resulted in a relatively vertical transition line.

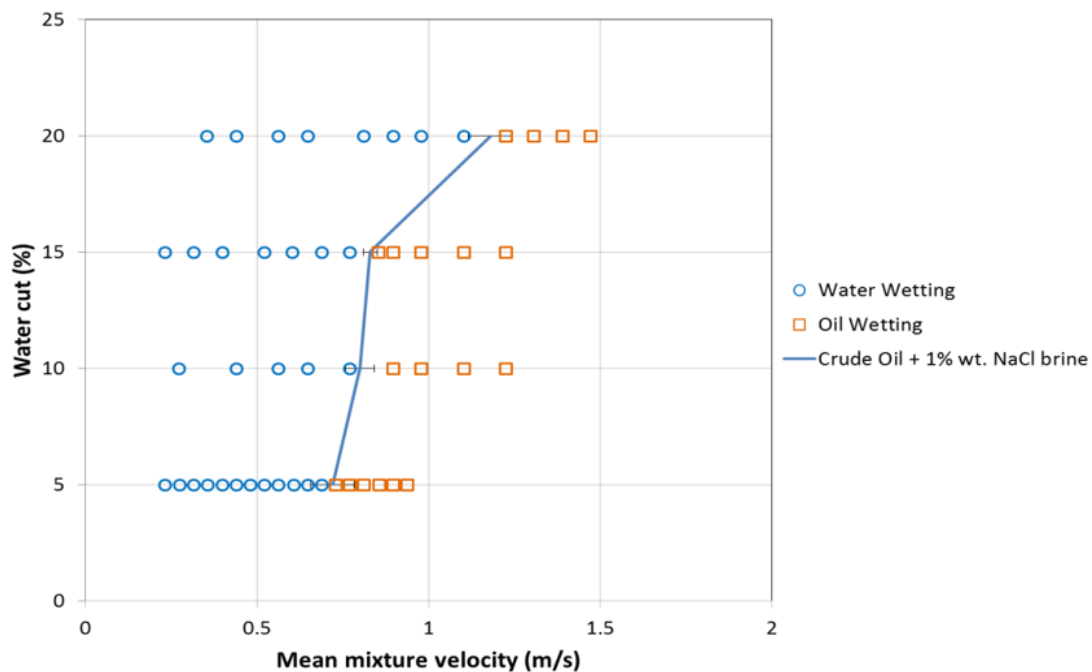


Figure 30. Phase wetting map of proprietary crude oil.

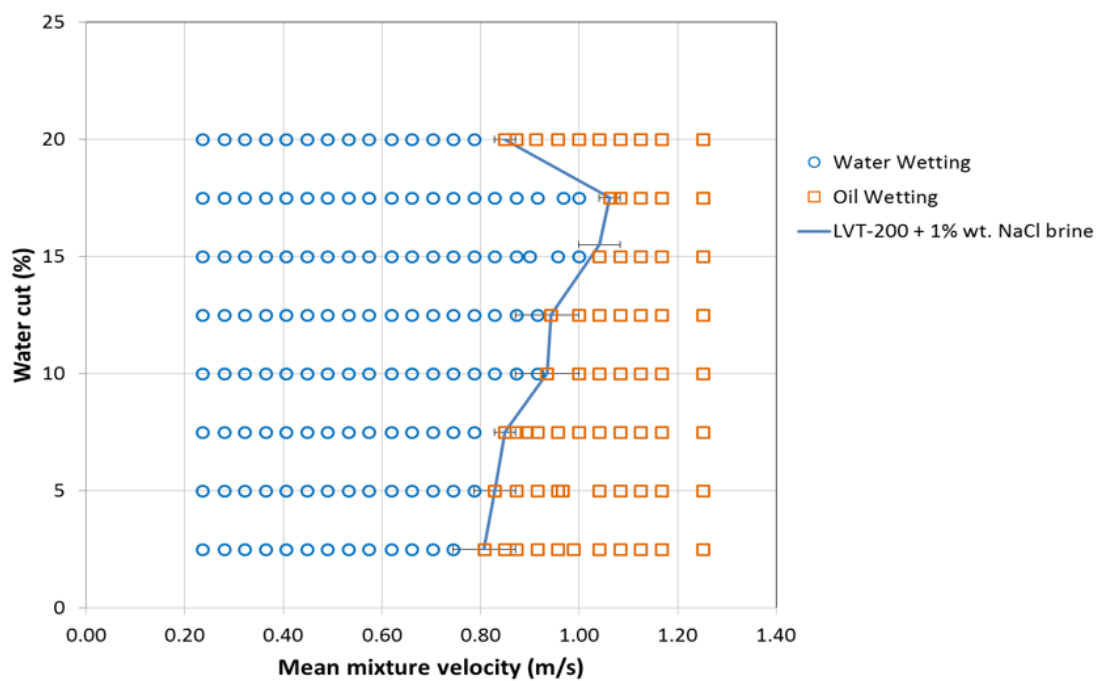


Figure 31. Phase wetting map of LVT-200 V.

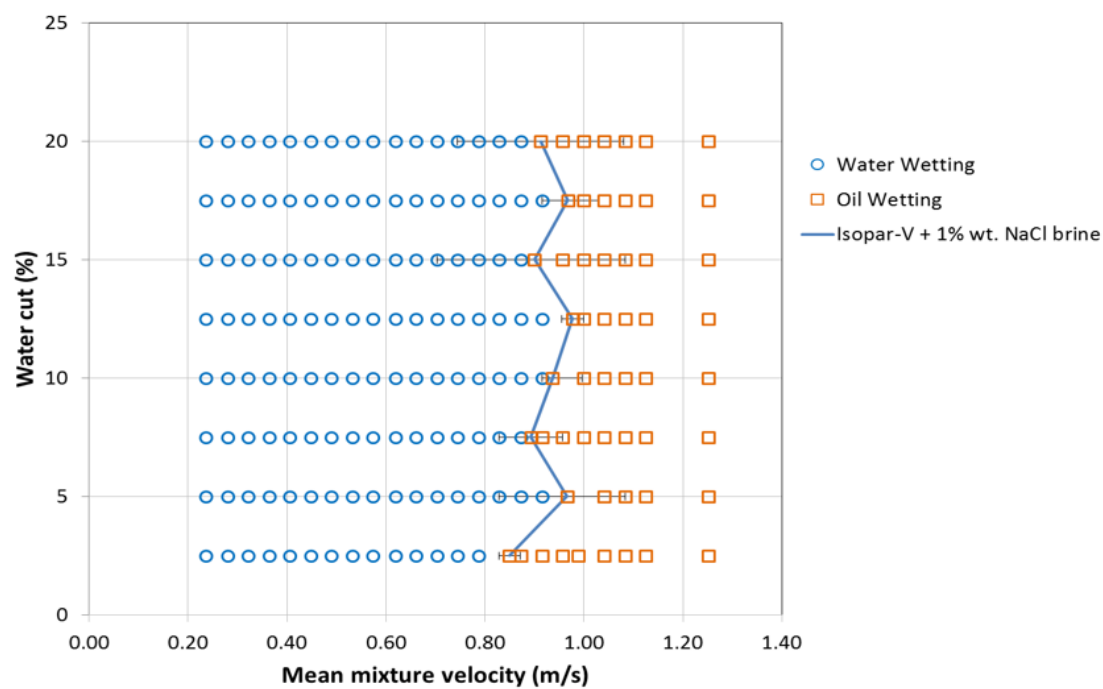


Figure 32. Phase wetting map of Isopar-V.

6.11. Determination of Blasius Type Correlations

This section presents the results of determining Blasius type correlations for Fanning friction factors, as outline in section 2.4. Fanning friction factors were determined using fluid properties, results of the CFD simulations, and the mean tangential velocity of the rotating top plate, U_T . The results of the CFD simulations were used to first calculate the Fanning friction factors. The Fanning friction factors were then plotted as a function of Reynolds number, and the Blasius type correlations were determined. Additionally, an experimental bottom Fanning friction factor was determined using experimental results of bottom wall shear stress. This experimental Fanning friction factor is shown for comparison purposes only as it is not believed that the experimentally measured bottom wall shear stress values are correct.

The resulting Blasius type relations are as follows.

$$f_{Top} = 1.0597Re^{-0.491} \quad (39)$$

$$f_{Bottom} = 0.1912Re^{-0.421} \quad (40)$$

$$f_{Bottom\ exp} = 2 \times 10^{-5}Re^{-0.157} \quad (41)$$

These relations, graphically depicted in Figure 33 (except for $f_{Bottom\ exp}$) can be used in subsequent calculations for the water wetting model of the annular flume without requiring any additional CFD simulations.

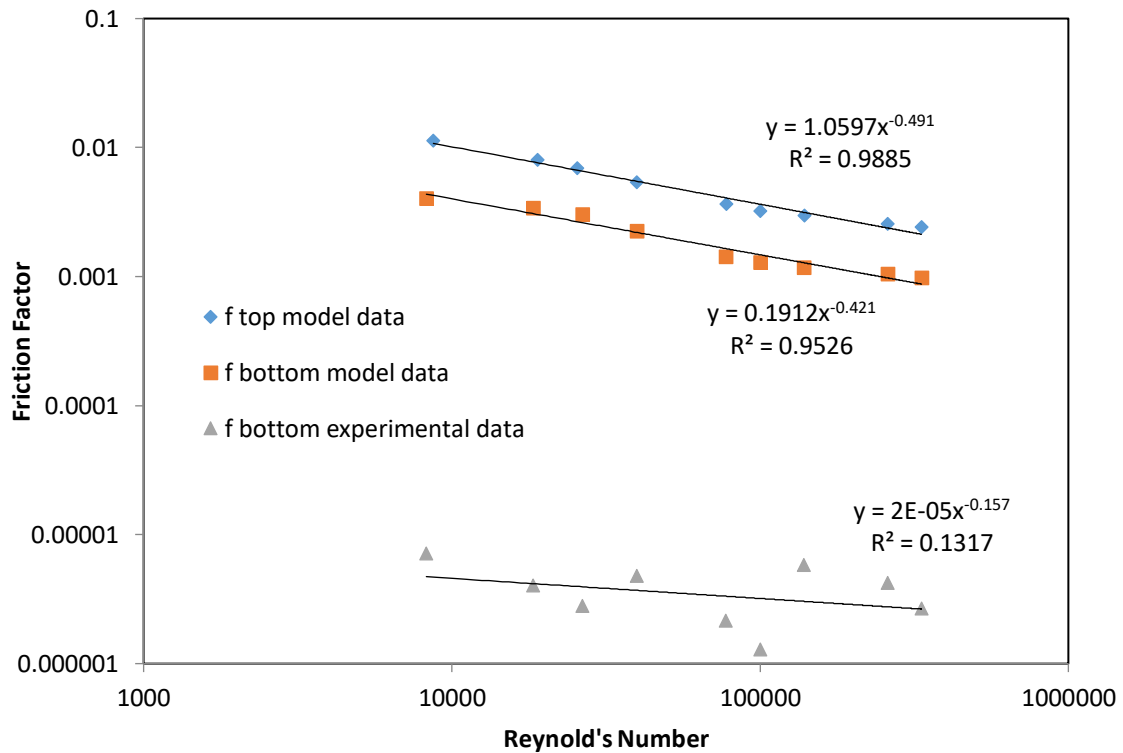


Figure 33. Plots of top friction factors and bottom friction factors as functions of Reynolds number on a logarithmic scale.

The trendline for the model data of f_{Bottom} and experimental data of $f_{Bottom\ exp}$ correlation coefficients of $R^2 = 0.9526$, and $R^2 = 0.01317$, respectively. The low correlation coefficient of the trendline of $f_{Bottom\ exp}$ is due to the high variability of the experimental measurements of bottom wall shear stress. Ideally, f_{Bottom} would be validated by comparing it to $f_{Bottom\ exp}$, and possibly developing some level of uncertainty in f_{Bottom} . Because the experimental results of $\tau_{WB\ exp}$ are being discarded due to their high variability, this cannot be done in the present study. Recommendations for proceeding with the Fanning friction factor results are discussed in the following section.

RECOMMENDATIONS

The following recommendations serve to advance comprehension of the hydrodynamics of the annular flume apparatus.

The temperature of the fluid during experimentation was not controlled nor monitored. Fluctuations in fluid temperature due to fluctuations in ambient temperature or experimentation may affect the results of the hydrodynamic studies. Additionally, during long periods of testing, fluids may experience heating due to heat transfer from the annular flume apparatus motor. A sufficiently large variation in fluid temperature during experimentation could result in a change in fluid physical properties that may affect hydrodynamic characteristics. The temperature of the experimental fluids should be controlled and monitored in future hydrodynamic and phase wetting experiments in the annular flume apparatus.

The high variability of the experimental results for bottom wall shear stress were most likely due to the bottom wall shear stress probe used in the experiments. The probe used had a measurement range of 0-140 Pa with a resolution of 5 Pa. Model results of bottom wall shear stress in the annular flume apparatus exhibited values as low as approximately 0.25 Pa and as high as approximately 21.00 Pa in the mid-radius of the conduit. As such, a wall shear stress suited for this range of measurement with a more refined resolution than the probe used in the present study should be tested in the annular flume apparatus to measure bottom wall shear stress.

CONCLUSIONS AND FUTURE WORK

The annular flume was characterized hydrodynamically. This was done by obtaining measurements of velocity and bottom wall shear stress in single phase flow of three different fluids, modeling single phase flow in the annular flume using the $k - \varepsilon$ turbulence model in CFD simulations, and then by validating these simulations using the results of hydrodynamic measurements of velocity and bottom wall shear stress. The CFD simulations aided in the calculation of friction factors used in the prediction of phase wetting regimes specific to the annular flume.

To validate the use of the $k - \varepsilon$ turbulence model used in the CFD simulations, CFD results of tangential velocity and bottom wall shear stress were compared with experimental results of tangential velocity and bottom wall shear stress, respectively. Experimental velocity measurements were acquired using a Pitot tube and differential transducer, and bottom wall shear stress measurements were acquired using a wall shear stress probe. Good agreement was found between the CFD results and the experimental results of tangential velocity. The standard error in the calibration curve was low (0.07 m/s).

Experimental results of bottom wall shear stress differed greatly from CFD results, by as much as an order of magnitude in some instances. This discrepancy, coupled with the unusually high measurement variability in the wall shear stress probe, inferred that the issue came from problems with the wall shear stress probe itself, rather than poor estimations of bottom wall shear stress by CFD simulations. Upon receiving guidance from the manufacturer on ways to possibly correct the problem, and observing

subsequent poor bottom wall shear stress measurements, it was determined that the probe, due to its specified measurement range (0 to 140 Pa) and resolution (5 Pa), may not be suitable for use in the annular flume, and that the experimental results for bottom wall shear stress would be discarded. Because of the good agreement between the CFD results and experimental results for tangential velocity, it was determined that the $k - \varepsilon$ model was appropriate for use in CFD simulations of the annular flume; subsequently the CFD simulations were used to characterize the annular flume. It is recommended that a wall shear stress probe suited for much lower values of shear (0 - ~25 Pa) be used for similar experiments in the future.

Due to the circular geometry of the annular flume and the means of flow induction via shear by a rotating top plate, the presence of a secondary cross flow was expected and observed in the CFD simulations. Specifically, this cross flow originates at the top plate, where centrifugal forces cause the fluid phase to flow towards the outer wall, down the outer wall, across the bottom plate towards the inner wall, and recirculate back towards the top plate.

Tangential velocity and transverse velocity throughout the conduit were visualized with contours and vector fields, respectively. Both tangential velocity and transverse velocity exhibit their largest values near the outer wall and the top plate. In general, tangential velocity increases with increasing radial position across the conduit, so this result was expected. This results in a bottom wall shear stress gradient across the conduit, as well.

Vector fields of transverse velocity helped visualize the cross flow that occurs within the conduit. It was initially suspected that the circular geometry of the annular flume could result in this secondary flow.

A Fanning friction factor of the top of the conduit, f_{Top} , and for the bottom of the conduit, f_{Bottom} were determined in this study, correlating Reynolds number and the respective friction factors using mean tangential velocity of the top plate, fluid properties, and values of top plate torque and bottom plate torque obtained from CFD simulations. Experimental results of bottom wall shear stress were used to determine a Blasius type correlation for an experimental Fanning friction factor, $f_{Bottom\ exp}$.

The Blasius type correlation for $f_{Bottom\ exp}$ had a correlation coefficient of $R^2 = 0.0132$ while the correlation for f_{Bottom} had a correlation coefficient of $R^2 = 0.9526$. The low correlation coefficient of $f_{bottom\ exp}$ is due to the high variability in the measurements of τ_{WBexp} . Because of these poor experimental results, it is not believed that $f_{Bottom\ exp}$ provides an accurate representation of the flow in the annular flume. The CFD generated f_{Bottom} should be used instead. Obtaining more accurate measurements of τ_{WBexp} may be possible if a wall shear stress probe suited for lower values of wall shear stress in the range of 0-25 Pa is tested in the annular flume apparatus. Until this is done, a value for the uncertainty in f_{Bottom} cannot be estimated.

Once the water wetting model is developed for the annular flume, future studies should use f_{Bottom} and f_{Top} in the prediction of phase wetting in the annular flume

apparatus for various fluids at multiple water cuts, and these predictions compared with phase wetting observations in the annular flume apparatus.

The CFD simulations performed in this study present an initial step in performing CFD simulations of multiphase flow in the annular flume. Future studies may aim to perform these CFD simulations of multiphase flow in the annular flume.

In addition, it was shown by Paolinelli et al. (Paolinelli et al., 2018) that the surface wettability of the interior surface of pipe flow heavily influences the phase wetting regime and the onset of fully dispersed flow. Future studies should aim to vary surface wettability by performing similar experiments as the present study with surfaces in addition to stainless steel. The hydrophobicity of stainless steel results in the onset of fully dispersed (oil wetting) flow occurring at lower flow velocities due to poor surface wettability (water wetting); whereas, the hydrophilicity of carbon steel results in enhanced surface wettability and much higher flow velocities required for full entrainment of water in oil. This should be explored further in the annular flume.

REFERENCES

- Avsarkisov, V., Hoyas, S., Oberlack, M., & Garcia-Galache, J. (2014). Turbulent plane Couette flow at moderately high Reynolds number. *J. Fluid Mech.*, 51, 21-24.
- Ayello, F. (2010). *Crude Oil Chemistry Effects on Corrosion Inhibition and Phase Wetting in Oil-Water Flow*. (PhD Dissertation). Ohio University, Athens, OH.
- Cai, J. Y., Nestic, S., Li, C., Tang, X., Ayello, F., Cruz, I., & Khamis, J. (2005, January 1) Experimental Studies of Water Wetting in Large Diameter Horizontal Oil-Water Pipe Flows. SPE Annual Technical Conference and Exhibition, October 9. Dallas, Texas.
- Cai, J., C. Li, X. Tang, F. Ayello, S. Richter, S. Nestic, (2012). Experimental Study of Water Wetting in Oil-water Two Phase Flow-Horizontal Flow of Model Oil. *Chemical Engineering Science*, 73, 334-444.
- Dean, W. R. (1928). The streamline motion of fluid in a curved pipe. *Phil. Mag.* 5(7), 673-695.
- de Dood, M.J.A. (1997). *Oil/water flow in a carousel* (MSc thesis), Technical Physics, University of Amsterdam, Amsterdam.
- Elseth, G., (2001). *An Experimental Study of Oil/Water Flow in Horizontal Pipes* (PhD Dissertation), Department of Technology. The Norwegian University of Science and Technology, Porsgrundh, Norway
- Gardner, T. Paolinelli, L., Nestic, S. (2017). *Study of water wetting in oil-water flow in small scale annular flume* (Unpublished thesis). Ohio University, Athens, Ohio.
- Graham, D., James, P., Jones, T., Davies, J., and Delo, E. (1992). Measurement and Prediction of Surface Shear Stress in Annular Flume. *J. Hydraul. Eng.*, 118(9), 1270-1286.
- Hernandez, Sandra E., S. Nestic. 2005. Use of artificial networks for predicting crude oil effect on CO2 corrosion of carbon steel. Presented at NACE Corrosion Conference, San Antonio, Texas, May 8th. Houston, Texas: NACE International. Paper #0554.
- Hinze, J. O. (1955). Fundamentals of the Hydrodynamic Mechanism of Splitting in Dispersion Processes. *A. I. Ch. E. Journal*, 1(3), 289-295.
- Kawahara, G., & Kida, S. (2001). Periodic motion embedded in plane Couette turbulence: Regeneration cycle and burst. *J. Fluid Mech.*, 449, 291-300.
- Kee, K. Richter, S., Babic, M., Nestic, S. (2014. March). Flow Patterns and Water Wetting in Oil-Water Two-phase Flow-A Flow Loop Study. Presented at NACE Corrosion Conference, San Antonio, Texas, March 13th. Houston, Texas: NACE International. Paper no. 6113.
- Kowalewski, E., T. Holt, and O. Torsaeter. (2002). Wettability alterations due to an oil soluble additive. *Journal of Petroleum Science & Engineering*, 33, 19-28.
- Kuei-Yuan Chien. (1982). Predictions of Channel and Boundary Layer Flows with a Low Reynolds Number Turbulence Model. *AIAA Journal*, 20(1), 33-38.
- Lee, A. H. (1993). *A Study of Flow Regime Transitions for Oil-Water-Gas Mixtures in Large Diameter Horizontal Pipelines* (M.S. thesis). Ohio University, Athens, OH.

- Li, C. (2009). *Effect of Corrosion Inhibitor on Water Wetting and Carbon Dioxide Corrosion in Oil-Water Two-Phase Flow* (Doctoral Dissertation). Ohio University, Athens, OH.
- Mlynek, Y., Resnick, W. (1972). Drop sizes in an agitated liquid-liquid system. *A. I. Ch. E. Journal*, 18, 122-127.
- NACE. (2016). International Measures of Prevention, Application, and Economics of Corrosion Technologies Study. Retrieved from <http://impact.nace.org/executive-summary.aspx>.
- Nordsveen, M., Nestic, S., Nyborg, R., & Stangeland, A. (2003). A mechanistic model for carbon dioxide corrosion of mild steel in the presence of protective iron carbonate films – Part I: Theory and verification. *Corrosion*, 59(5), 443-456.
- Papavassiliou, D., & Hanratty, T. (1997). Interpretation of large-scale structures observed in a turbulent plane Couette flow. *International Journal of Heat and Fluid*, 18, 55-69.
- Paul, H., Scleicher, C. (1965). The maximum stable drop size in turbulent flow: Effect of pipe diameter. *Chemical Engineering Science*, 403, 57-59.
- Paolinelli, L., Rashedi, A., Yao, j., Singer, M. (2018). Study of water wetting and water layer thickness in oil-water flow in horizontal pipes with different wettability. *Chemical Engineering Science*, 183, 200-214.
- Ragil, K., Bonn, D., Broseta, D., Indekeu, J., Kalaydjian, F., Meunier, J. (1998). The wetting behavior of alkanes on water. *Journal of Petroleum Science & Engineering*, 20, 177-183.
- Schiller, L., Naumann, A., (1933). About the basic calculations in Schwefkraftaubereitung. *The Association of German Engineers Journal*, 77, 318–320.
- Segev, A., 1985. Mechanistic Model for Estimating Water Dispersion in Crude Oil Flow. Presented at Annual AIChE Meeting, San Francisco, CA, Nov. 25th, United States: AIChE.
- Selker, A., Sleicher, Jr., C.A. (1965). Factors affecting which phase will disperse when immiscible liquids are stirred together. *Can. J. Chem. Eng.*, 43 (6), 298-301.
- Sheverev, V. A., & Stepaniuk, V. (2012). U.S. Patent No. US8276463. Washington, DC: U.S. Patent and Trademark Office.
- Shoham, O. (2006). *In Mechanistic Modeling of Gas-Liquid Two-Phase Flow in Pipes*. Houston, Texas: Society of Petroleum Engineers.
- Gardner, T., Paolinelli, L., Nestic, S. (2018). *Study of water wetting in oil-water flow in small-scale annular flume* (Unpublished thesis). Ohio University, Athens, Ohio.
- Versteeg, H. K., Malalasekera, W. (2007). *An Introduction to Computational Fluid Dynamics: The Finite Volume Method 2nd Edition*. London: Pearson.
- Vieth, P. H., Roytman, I., Mesloh, R. E., Kiefner, J.F. (1996). *Analysis of DOT-Reportable Incidents for Gas Transmission and Gathering Pipelines* Contract No. PR-218-9406 January 1, 1985 through December 31, 1995. Lock Haven, Pa: Kiefner & Associates.

- de Waard, C., Smith, L., Craig, B.D. (2001). The Influence of Crude Oil on Well Tubing Corrosion Rates. Paper presented at NACE Corrosion Conference, San Antonio, Texas, March 2003. Houston Texas: NACE International. Paper no. 03629.
- Yang, Z., Baptista, A., & Darland, J. (2000). Numerical modeling of flow characteristics in rotating annular flume. *Dynamics of Atmospheres and Oceans*, 33(4), 271-294.
- Yao, J. (2016). *Characterization and prediction of droplet size in oil/water flow* (Master's Thesis). Ohio University, Athens, OH.
- Zuidema, H. H., Waters, G. W. (1941). Ring Method for the Determination of Interfacial Tension. *Industrial and Engineering Chemistry (Analytical Edition)*, 13(5), 312-313.

APPENDIX 1: $k - \epsilon$ TURBULENCE MODEL

The following equations describe the standard $k - \epsilon$ turbulence model that was used in the CFD simulations. It is assumed that the turbulent viscosity is isotropic.

For turbulent kinetic energy k , the equation below shows that the rate of change of k and the transport of k by convection is equal to the transport of k by diffusion plus the rate of production of k minus the rate of destruction of k .

$$\frac{\partial(\rho k)}{\partial t} + \frac{\partial(\rho k u_i)}{\partial x_i} = \frac{\partial}{\partial x_j} \left[\frac{\mu_t}{\sigma_k} \frac{\partial k}{\partial x_j} \right] + 2 \mu_t E_{ij} E_{ij} - \rho \epsilon \quad (42)$$

Where $\rho =$ density of the bulk material

$t =$ time

$x_i =$ position in the corresponding direction

$u_i =$ velocity component in corresponding direction

$E_{ij} =$ rate of deformation

$$\mu_t = \rho C_\mu \frac{k^2}{\epsilon}$$

For dissipation ϵ , the equation below shows that the rate of change of ϵ and the transport of ϵ by convection is equal to the transport of ϵ by diffusion plus the rate of production of ϵ minus the rate of destruction of ϵ (Versteeg & Malalasekera, 2007).

$$\frac{\partial(\rho \epsilon)}{\partial t} + \frac{\partial(\rho \epsilon u_i)}{\partial x_i} = \frac{\partial}{\partial x_j} \left[\frac{\mu_t}{\sigma_\epsilon} \frac{\partial \epsilon}{\partial x_j} \right] + C_{1\epsilon} \frac{\epsilon}{k} 2 \mu_t E_{ij} E_{ij} - C_{2\epsilon} \rho \frac{\epsilon^2}{k} \quad (43)$$

Where $C_\mu = 0.09$,

$$\sigma_k = 1.00$$

$$\sigma_\epsilon = 1.30$$

$$C_{1\epsilon} = 1.44$$

$$C_{2\epsilon} = 1.92$$

These constants have been determined for a range of turbulent flows (Versteeg & Malalasekera, 2007).

APPENDIX 2: CALCULATION OF VERTICAL VELOCITY COMPONENT OF TRANSVERSE FLOW

This section serves to outline the process of using results from this study in determining key velocity values used in the water wetting model developed by Dr. Paolinelli at Ohio University. Figure 34 shows a plot of vertical velocity, U_y , at varying heights at mid-width of the conduit. Determining the mean vertical velocity, U_{ym} , is accomplished by integrating U_y across the height of the conduit. The dimensionless wall coordinate, y^+ , is used to define these sections, and in subsequent calculations, in order to normalize results. The equation for the wall coordinate, y^+ , is shown in the following equation.

$$y^+ = \frac{y\rho_c U_B^*}{\mu_c} \quad (44)$$

Where y (m) is the distance from the bottom of the conduit, and U_B^* , the friction velocity (m/s) at the bottom of the conduit is defined by the following equation.

$$U_B^* = \sqrt{\frac{\tau_{WB}}{\rho_c}} \quad (45)$$

It is assumed that a droplet in the annular flume is spherical, implying that its center of mass lies at half its diameter. The y^+ coordinate corresponding to center of mass of a droplet is denoted $y^+ \left(\frac{d}{2}\right)$. Thusly, the U_{ym} experienced by a droplet is estimated based on $y^+ \left(\frac{d}{2}\right)$.

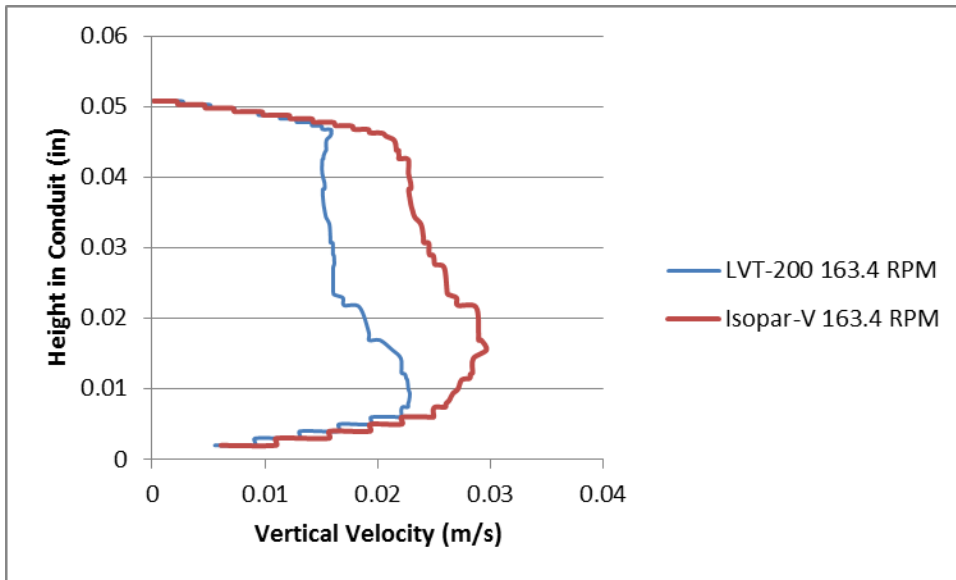


Figure 34. Plots of vertical velocity for LVT-200 and Isopar-V at 163.4 RPM.

These values of U_{ym} are determined using the friction velocity at the top of the conduit, U_T^* , defined as follows.

$$U_T^* = \sqrt{\frac{\tau_{WT}}{\rho_c}} \quad (46)$$

Using the results of the CFD simulations, the following equation describes the linear relation between U_{ym} , and U_T^* .

$$U_{ym} = U_T^*(0.001 y^+ + 0.054); \quad (47)$$

Which is valid under the following criteria,

$$1500 < Re < 350000; 5 < y^+ < 120$$



OHIO
UNIVERSITY

Thesis and Dissertation Services